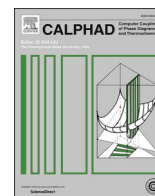




Contents lists available at ScienceDirect

Calphad

journal homepage: www.elsevier.com/locate/calphad

Investigation of the solid/liquid phase transitions in the U–Pu–O system

P. Fouquet-Métivier^a, P.M. Martin^a, D. Manara^{b,*}, K. Dardenne^c, J. Rothe^c, P.C.M. Fossati^d, C. Guéneau^d

^a CEA, DES, ISEC, DMRC, Université Montpellier, Marcoule, BP1717, 30207, Bagnols-sur-Cèze, France

^b European Commission, Joint Research Centre, Via Enrico Fermi 2749, 21027, Ispra, Italy

^c Institut für Nukleare Entsorgung (INE), Karlsruhe Institute of Technology, Hermann Von Helmholtz Platz 1, 76344, Eggenstein-Leopoldshafen, Germany

^d Université Paris-Saclay, CEA, Service de la Corrosion et du Comportement des Matériaux dans leur Environnement, 91191, Gif-sur-Yvette, France

ARTICLE INFO

Handling editor: Prof. Z.K. Liu

Keywords:

Solid/liquid phase transitions

Thermodynamic modelling

Oxygen stoichiometry

$U_{1-y}Pu_yO_{2\pm x}$

Nuclear safety

ABSTRACT

Mixed oxides of uranium and plutonium $U_{1-y}Pu_yO_{2-x}$ are currently studied as reference fuel for Sodium-cooled Fast Reactors (SFRs). To predict the margin to fuel melting, an accurate description of both solidus and liquidus temperatures of these materials is crucial. In this work, after a critical review of the literature data, the parameters of the liquid phase of the CALPHAD models of the Pu–O and U–Pu–O systems are reassessed based on the model of Guéneau et al.. A good agreement between the calculated and selected experimental data is obtained. Using this model, the melting behaviour of $U_{1-y}Pu_yO_{2\pm x}$ oxides is then studied as a function of plutonium content and oxygen stoichiometry. The congruent melting for the mixed oxides is found to be shifted towards low O/M ratios compared to the end-members ($UO_{1.97}$ and $PuO_{1.95}$). The temperature of this congruent melting is nearly constant (3130–3140 K) along a ternary phase boundary from $UO_{1.98}$ to $U_{0.55}Pu_{0.45}O_{1.82}$ and then decreases with Pu content to a maximum of approximately 3040 K for $PuO_{1.95}$. This observation is explained by the stabilisation of the hypo-stoichiometric mixed oxides due to the increase of the configurational entropy at high temperatures by the formation of oxygen vacancies and related cation mixing. The influence of the atmosphere used in the laser heating melting experiments on the oxygen stoichiometry of the sample and its solidus and liquidus temperatures is investigated. The determination of this O/M ratio after laser melting tests using XANES is also reported. The simultaneous presence of U^{6+} , U^{5+} , U^{4+} , Pu^{3+} and Pu^{4+} is observed, highlighting the occurrence of charge compensation mechanisms. The samples are highly oxidised in air whereas close to stoichiometry ($O/M = 2.00$) in argon. These results are in agreement with the computed solidification paths. This work illustrates the complex melting behaviour of the $U_{1-y}Pu_yO_{2\pm x}$ fuels and highlights the need for the CALPHAD method to accurately describe and predict the high-temperature transitions of the U–Pu–O system.

1. Introduction

Mixed oxide $U_{1-y}Pu_yO_{2-x}$ fuels are currently studied within the framework of the development of fourth-generation (GEN-IV) Sodium-cooled Fast Reactors (SFR) [1]. An accurate knowledge of the thermodynamic and structural properties of these fuels is essential to predict their behaviour during operation. Indeed, the temperature can reach up to 2200 K in normal operating conditions at the centre of the fuel pellet, whereas it remains around 773 K close to the cladding [2]. This large temperature gradient along 2–2.5 mm within the fuel pellet causes the redistribution of oxygen and metals atoms under irradiation. Moreover, the initial O/M (Oxygen/Metal) ratio of the fuel must range between 1.94 and 1.99. The lower limit is set to prevent an insufficient thermal

conductivity of the mixed oxide that could lead to the fuel melting. The upper limit is fixed to minimise the corrosion of the stainless-steel cladding. Upon irradiation, due to oxygen redistribution, the O/M ratio also varies within the pellet being low at its centre (associated with a higher Pu content) and close to 2.00 near the rim and close to the cladding (associated with a lower Pu content) [2]. Thus, an accurate knowledge and prediction of the solid to liquid transition temperatures is important to assess the melting fuel behaviour in a wide range of O/M and Pu content, denoted y, under normal operating conditions but also in case of severe accidents. However, the determination of these data as a function of plutonium content and O/M ratio still represents an experimental challenge, despite improvements over the last decades [3–5].

* Corresponding author.

E-mail address: dario.manara@ec.europa.eu (D. Manara).

<https://doi.org/10.1016/j.calphad.2022.102523>

Received 15 September 2022; Received in revised form 13 December 2022; Accepted 18 December 2022

0364-5916/© 2022 The Authors. Published by Elsevier Ltd. This is an open access article under the CC BY license (<http://creativecommons.org/licenses/by/4.0/>).

The TAF-ID (Thermodynamics of Advanced Fuel-International Database) project [6] was initiated to develop a comprehensive thermodynamic database on nuclear fuel materials. In this work, the CALPHAD model published by Guéneau et al. in 2011 on the U–Pu–O system was introduced to describe the thermodynamic properties of $U_{1-y}Pu_yO_{2\pm x}$ mixed oxides and the phase diagram of the U–Pu–O system [7]. Since then, other sets of solidus and liquidus temperatures for $U_{1-y}Pu_yO_{2\pm x}$ were obtained experimentally after 2011 [5,8,9], highlighting the need for a re-assessment of the model of the U–Pu–O system.

The goal of this work is thus to propose an improved thermodynamic model of the U–Pu–O system to better reproduce the available experimental data and discuss the influences of several parameters such as the plutonium content or the O/M ratio on the melting behaviour of $U_{1-y}Pu_yO_{2\pm x}$ mixed oxides.

This work first consists in a critical review of the available experimental data on solid to liquid transition temperatures in the Pu–O and U–Pu–O systems. Then the CALPHAD model of Guéneau et al. is updated for the liquid phase only, to take into account these new datasets. Thermodynamic calculations are performed to explain the position of the congruent melting temperature curve in the ternary. Post-melting characterisations by XANES of O/M ratio are reported for $U_{1-y}Pu_yO_{2.00}$ samples molten under either air or argon by Strach et al. [9]. The influence of the atmosphere on the change in the O/M ratio and on the solidus/liquidus temperatures is then determined and compared to calculated solidifications paths using our model. Finally conclusive remarks and perspectives are presented.

These calculations were performed in the framework of the INSPYRE H2020 project [10].

2. Critical review and selection of the experimental solidus/liquidus data

The modelling of the U–Pu–O system is based on the assessment of its binary sub-systems. As no new solidus and liquidus temperatures were reported on U–Pu and U–O systems since 2011, the state of the art of the experimental data is here presented only for the Pu–O and U–Pu–O systems.

2.1. Pu–O

A first review of the available measurements of the PuO_2 melting point (by thermal arrest technique) was performed in 2001 by Carbajo et al., who recommended the value of 2701 ± 35 K [11]. In 2008, a higher value (2822 K) was obtained by Kato et al. using the same experimental approach but with a Re crucible [4,12]. However, the authors reported some interactions between the crucible and the $PuO_{2.00}$ sample, suggesting an inaccurate melting point determination. In 2011, using a laser heating set-up and a self-crucible strategy developed by Manara et al. [13], De Bruycker et al. [12] measured the melting point of PuO_2 at 3017 ± 28 K. In their critical review of the melting point measurements performed until 2011 for PuO_{2-x} , Konings et al. [14] discarded the values obtained by thermal arrest technique and recommended the use of the value determined by De Bruycker et al.. This value was adopted by Guéneau et al. in their CALPHAD assessment [7].

In 2014, Böhler et al. measured a higher melting point for $PuO_{2.00}$ at 3050 ± 59 K [5], using the same laser heating technique.

In the PuO_{2-x} domain, only one experimental study is reported in the literature. Indeed, Kato et al. [15] measured a melting temperature of 3031 ± 20 K for $PuO_{1.76}$ using a thermal arrest technique. The authors concluded that the melting temperature was at a maximum at this composition. The melting temperature then decreased as the samples were closer to their stoichiometric composition PuO_2 .

It can be noticed that the temperature obtained for $PuO_{1.76}$ (3031 ± 20 K) is very close to that measured by Böhler et al. for $PuO_{2.00}$ (3050 ± 59 K). However, care should be taken while analysing these values, as they originate from two different techniques: thermal arrest using Re

crucible and laser heating with a self-crucible system, respectively.

Indeed, when using classical thermal analysis, interactions between PuO_2 and its containers due to its high oxygen potential were always noticed. The result of this interaction is an underestimated melting temperature [12]. Moreover, even with a closed crucible, considering the longer time needed to perform the experiments (few hours), a change in the composition of the sample could have occurred at high temperatures due to noncongruent vaporisation. Unfortunately, no post-melting characterisations were reported.

In the case of the laser heating technique, shorter experiment durations were reported (100–500 ms). However, the exact oxygen stoichiometry of the sample during the melting remains uncertain, as vaporisation can also occur. Again, no experimental determination of the exact stoichiometry of the molten PuO_2 samples was performed.

Based on the literature review performed here, the melting point of Böhler et al. (3050 ± 59 K) was selected for $PuO_{2.00}$ [5]. Indeed, compared to the one of De Bruycker et al. using the same technique (3017 ± 28 K) [16], it is considered as the most reliable value as the authors improved the experimental conditions to ensure the mechanical stability of the sample and the repeatability of the measurements.

For Pu_2O_3 , the melting point recommended by Konings et al. [14] is 2352 ± 10 K, based on the consistent measurements of Chikalla et al. [17] and Riley [18]. The few scattered solidus/liquidus measurements performed between Pu_2O_3 and PuO_2 were not selected as uncertainties remain on the final sample composition [19]. Nevertheless, some of these melting points will be reported on the calculated phase diagram for comparison.

2.2. U–Pu–O

In this section, only studies on fresh $U_{1-y}Pu_yO_{2\pm x}$ will be presented, as irradiated fuels are beyond the scope of this present work.

The melting behaviour of the uranium-plutonium mixed dioxides has been extensively studied over the past decades by Lyon and Baily [20], Aitken and Evans [3], Reavis [21], Konno and Hirose [22], Kato et al. [4,19] using methods based on high temperature furnaces and later by De Bruycker et al. [8], Böhler et al. [5] and Strach et al. [9] using laser heating. Reviews of the literature data were performed by Kato et al. in 2009 [23] and Guéneau et al. in 2011 [7]. The composition range and the methods for the available measurements are reported in Table 1. The experimental data are shown in Fig. 1, where only stoichiometric dioxides, with an O/M ratio equal to 2.00, are represented for the sake of clarity. Large discrepancies can be noticed for both solidus and liquidus temperatures.

The first measurements on $U_{1-y}Pu_yO_{2-x}$ samples were performed by Lyon and Baily ($0 < y \leq 0.85$, O/M = 2.00), followed by Aitken and Evans ($0.20 \leq y \leq 0.60$), using a thermal arrest technique on stoichiometric samples encapsulated in tungsten crucibles [3,20]. Their results were well described by an ideal solution model between UO_2 and PuO_2 , with a melting point of PuO_2 around 2700 K and an increase of the solidus temperatures when decreasing the PuO_2 content. In the study of Aitken and Evans, hypo-stoichiometric fuels were also studied with the same technique, in the range $1.76 \leq O/M \leq 2.00$ and $0.2 < y \leq 0.6$ [3]. The maximum melting temperature was observed for the lowest O/M ratio with values well below 2 (with for example 1.75 for PuO_{2-x}). The authors explained this behaviour by the stabilisation of the solid mixed oxides due to the Pu^{3+} and Pu^{4+} interaction in the hypo-stoichiometric region.

Reavis et al. studied the effect of the burn-up on the melting temperature of $U_{0.75}Pu_{0.25}O_{2-x}$ with $x = 0.02$ and 0.03 , using a differential thermal analysis method [25]. Their results on fresh fuels were found to be in agreement with the one of Aitken and Evans. Konno and Hirose also used a thermal arrest technique with W crucibles to measure the melting point of $U_{0.71}Pu_{0.29}O_{2-x}$ with $x = 0.01$ and 0.05 [22].

In 2008, Kato et al. performed measurements on samples with $0.117 \leq y \leq 0.60$ and $1.922 \leq O/M \leq 2.00$ using a thermal arrest method and

Table 1
Experimental solidus and liquidus data for fresh $U_{1-y}Pu_yO_{2\pm x}$ available in the literature.

Reference	Composition	Experimental technique	Selected for the re-assessment
Lyon and Baily (1967) [20]	$0 < y \leq 0.85$ O/M = 2.00	Thermal arrest technique using a sealed W crucible	No
Aitken and Evans (1968) [3]	$0.20 \leq y \leq 0.60$ $1.76 \leq O/M \leq 2.00$	Thermal arrest technique using a sealed W crucible	No
Reavis (1972) [21]	$y = 0.25$ O/M = 1.97 and 1.98	Differential Thermal Analysis using W crucible	No
Konno and Hirose (1998) [24]	$y = 0.29$ O/M = 1.95 and 1.99	Thermal arrest technique using a sealed W crucible	No
Kato et al. (2008) [4, 15,19]	$0.117 \leq y \leq 0.60$ $1.922 \leq O/M \leq 2.00$	Thermal arrest technique using sealed W or Re crucible	Yes for $y < 0.50$
De Bruycker et al. (2011) [8]	$0.75 \leq y \leq 0.90$ O/M = 2.00	Laser heating technique under Ar and air using a self-crucible system	No
Böhler et al. (2014) [5]	$0.037 \leq y \leq 0.90$ O/M = 2.00	Laser heating technique under Ar (low Pu contents) and air (high Pu contents) using a self-crucible system	Yes
Strach et al. (2016) [9]	$0.14 \leq y \leq 0.62$ O/M = 2.00	Laser heating technique under Ar and air using a self-crucible system	No

W crucibles [4]. However, as for PuO_{2-x} , interactions between the container and the samples were reported for $y > 0.20$ [4]. To avoid this phenomenon, Kato et al. conducted new measurements using Re capsules [19]. However, some chemical interactions were still observed for Pu content above $y > 0.5$. The solidus and liquidus temperatures were higher by 100 K compared to those with W crucibles. An ideal solution model was derived with a PuO_2 melting point of 2843 K, as described in Ref. [19]. Measurements on hypo-stoichiometric fuels were also performed in the same [19]. An increase of the solidus and liquidus temperatures was observed when the O/M ratio decreased from 2 to approximately 1.9. In all the studies of Kato et al., small fractions of Am resulting from the β -decay of ^{241}Pu were systematically found in the $U_{1-y}Pu_yO_{2-x}$ samples.

Solidus and liquidus temperatures were later measured on $U_{1-y}Pu_yO_{2-x}$ mixed oxides using the laser heating technique and self-

crucible system developed by Manara et al. [26]. Similarly to the PuO_2 samples, the $U_{1-y}Pu_yO_{2-x}$ samples were held by means of graphite screws in a sealed autoclave and the surface of the samples were melted under controlled atmospheres (argon for low Pu content or air for high Pu content). This technique was first used in 2011 by De Bruycker et al. for stoichiometric samples with $0.75 < y < 0.90$. As for PuO_2 , the measured solidus and liquidus temperatures were found much higher than those obtained by Kato et al. using thermal arrest [8]. Furthermore, the results of De Bruycker et al. were not consistent with the ideal solution model previously proposed by Kato et al.. In fact, the melting temperatures were found to be the lowest between $y = 0.50$ and 0.80 . In 2014, Böhler et al. performed further investigations using the same laser heating technique on stoichiometric samples over the whole plutonium content range [5]. One difficulty encountered was that in some cases, a single transition temperature was recorded during the sample cooling. It was then difficult to attribute the phase transition to a liquidus or a solidus temperature [8,27]. However, as proposed by Böhler et al., the single thermal arrest was attributed to the solidus temperature as this transition is the most energetic one [5]. A minimum in the solidus/liquidus curve was also observed between $y = 0.40$ and 0.70 . The results obtained for plutonium fractions below 0.50 were found to be in good agreement with those of Kato et al. [4] whereas deviations were observed for higher Pu contents. More recently, using the same set-up, Strach et al. performed additional measurements of solidus and liquidus temperatures for stoichiometric samples with $0.14 \leq y \leq 0.62$ [9]. The results are in agreement with the data of De Bruycker et al. and Böhler et al.. For low Pu content, the experiments were performed both under argon and air (blue and green circles in Fig. 1 respectively), and significantly lower solidus temperatures were noticed in air for all Pu contents except $y = 0.65$. As an example, a melting temperature of 2470 K was obtained in air, compared to 3065 K in argon for a Pu content $y = 0.14$ [9]. This was explained by the progressive oxidation of the samples along the successive shots. Nevertheless, the results obtained under Ar are in agreement with the values obtained by De Bruycker et al. and Böhler et al..

The influence of several parameters on the solid to liquid phase transitions can be highlighted in these studies:

- As for PuO_2 , the $U_{1-y}Pu_yO_{2.00}$ samples interacted with tungsten crucibles, explaining that lower melting temperatures are systematically obtained using thermal arrest techniques. Even with rhenium crucibles, some interactions were found for $y > 0.5$. Thus, these experimental data are not selected for the reassessment of the model.

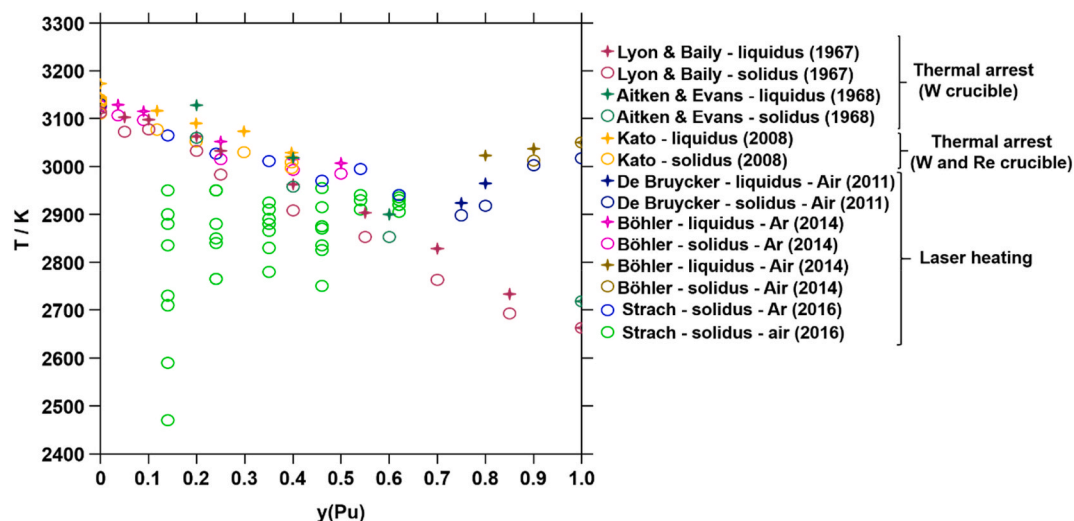


Fig. 1. Experimental melting data available in the literature for $U_{1-y}Pu_yO_2$.

- Plutonium content affects the solidus and liquidus temperatures. Contrarily to what was previously admitted, a non-ideal behaviour between UO_2 and PuO_2 is observed when using laser heating, with a minimum of the melting temperature located between $y = 0.40$ and 0.80 .
- The O/M ratio also influences the melting temperatures. The maximum of the melting temperature is determined at low O/M ratios (<1.9 by Kato et al. [19]), contrarily to what was reported in the U–O and Pu–O systems, where the congruent melting is found for O/M ratios close to 2.
- The influence of the atmosphere in the laser heating tests was also highlighted. Uranium-rich samples tend to oxidise under air, which leads to a progressive decrease of the melting temperature [9]. In case of Pu rich samples, air was used to maintain the O/M ratio close to 2.
- In the studies of De Bruycker et al. [8] and Böhler et al. [5], the final O/M ratio value was assessed at room temperature, after melting under argon and air, by combining XRD, XANES, and Raman spectroscopy measurements. Based on their findings, a final O/M ratio close to 2 or slightly below was determined. Unfortunately, no *in-situ* measurements of the O/M ratio at high temperature are available. Thus, the exact O/M ratio at which the solid/liquid transition occurs is still unknown.

In conclusion, as indicated in Table 1, the following data were selected for the re-assessment:

- For $y < 0.50$, the melting temperatures measured by Kato et al. [23] using Re crucibles and containing less than 1 at.% Am were used, as well as the data determined by Böhler et al. [5] using laser heating;
- For $y > 0.50$, only the measurements of Böhler et al. [5] were considered and preferred compared to the former results of De Bruycker et al. [8]. Data of Strach et al. obtained using the same technique were omitted due to the lack of detailed information in Ref. [9].

The solidus and liquidus temperatures measured by Kato et al. [23] and Böhler et al. [5], as well as the O/M ratios and Pu contents of these samples, selected for the re-assessment performed in this work can be found in Table 3 (Appendix).

3. Thermodynamic modelling

The starting point of this reassessment is the model developed by Guéneau et al. in 2011 [7]. Indeed, additional melting experiments were performed since this last re-assessment with a better control of the experimental conditions, giving new inputs for the thermodynamic modelling. In addition, a better description of the melting behaviour as a function of the O/M ratio was given experimentally by Kato et al. [23] and was needed to be considered in the re-assessment performed in this work.

The CALPHAD method was used in this work. The latter is commonly used to build a database containing the Gibbs energies of all the solid, liquid and gas phases as a function of temperature, composition and pressure [28]. In the present work, the Thermo-Calc software (version 2020b) was used [29]. Based on the solidus and liquidus experimental data selected in Section 2, only the parameters of the liquid phase for the Pu–O and the U–Pu–O systems will be modified. For the U–Pu and U–O sub-systems, the last versions of the models of Kurata [30] and Guéneau et al. [7], are used respectively, without modification.

In this section, the Gibbs energy model of the liquid phase will be first described. Then the re-evaluation of the Pu–O system will be presented. Finally, based on this re-evaluation, the reassessment of the model parameters for the liquid phase of the U–Pu–O system will also be described. The reassessed thermodynamic parameters are reported in Annex 1.

3.1. Gibbs energy model for the liquid

All the Gibbs energy functions are referred to the enthalpy of the pure elements in their stable standard state (standard element reference, SER), *i.e.* at 298.15 K and at 1 bar.

To describe the liquid phase of a metal-oxide system, the ionic two-sublattices model is used [31], represented by

$$(C_i)_P(A_j, Va^{Q-}, B_k)_Q \quad (1)$$

In this model, the first sublattice contains a mixture of cations (C_i) whereas anions (A_j , here O^{2-}), charged vacancies Va^{Q-} and neutral species (B_k) are introduced in the second sublattice.

For each metallic element, the oxidation state of the cation is chosen to be that of the cation in the first stable oxide compound to form in the system. For example, for Pu–O, Pu^{3+} is selected as Pu_2O_3 is the first oxide to form in the binary system. Pu^{4+} could have been added in the first sublattice but it is not recommended, as having several oxidation states for an element in the first sublattice can lead to the formation of metastable miscibility gaps. Thus, PuO_2 was added as a neutral species in the second sublattice.

In order to maintain the electrical neutrality of the liquid phase, the site numbers P and Q are defined as the average charges on the opposite sublattice

$$P = \sum_{A_j} v_{A_j} y_{A_j} + Q y_{Va} \quad (2)$$

$$Q = \sum_{C_i} v_{C_i} y_{C_i} \quad (3)$$

where v_i is the charge of species i , y_i corresponds to its site fraction, C_i stands for any cation and A_j for any anion. The sum of the constituent site fractions in each sublattice is equal to one.

The corresponding Gibbs energy (4) is described by the sum of three terms:

$$G^{\text{liq}} = {}^{\text{ref}}G^{\text{liq}} + {}^{\text{id}}G^{\text{liq}} + {}^{\text{exc}}G^{\text{liq}} \quad (4)$$

The reference term ${}^{\text{ref}}G^{\text{liq}}$ is defined as

$${}^{\text{ref}}G^{\text{liq}} = \sum_C \sum_A y_C y_A {}^0G_{(C)(A)}^{\text{liq}} + Q y_{Va} \sum_C y_C {}^0G_{(C)}^{\text{liq}} + Q \sum_B y_B {}^0G_{(B)}^{\text{liq}} \quad (5)$$

where ${}^0G_{(C)(A)}^{\text{liq}}$ represents the Gibbs energy of $(v_A + v_C)$ moles of liquid Cv_AAv_C , ${}^0G_{(C)}^{\text{liq}}$ the Gibbs energy of the pure liquid C and ${}^0G_{(B)}^{\text{liq}}$ the Gibbs energy of the liquid neutral species B .

The ideal term ${}^{\text{id}}G^{\text{liq}}$ corresponds to the configurational entropy on each sublattice:

$${}^{\text{id}}G^{\text{liq}} = RT \left[P \sum_C y_C \ln y_C + Q \left(\sum_A y_A \ln y_A + y_{Va} \ln y_{Va} + \sum_B y_B \ln y_B \right) \right] \quad (6)$$

The excess term ${}^{\text{exc}}G^{\text{liq}}$ is

$$\begin{aligned} {}^{\text{exc}}G^{\text{liq}} = & \sum_{C_1} \sum_{C_2} \sum_A y_{C_1} y_{C_2} y_A L_{(C_1, C_2)(A)}^{\text{liq}} + \sum_{C_1} \sum_{C_2} y_{C_1} y_{C_2} y_{Va}^2 L_{(C_1, C_2)(Va)}^{\text{liq}} \\ & + \sum_C \sum_{A_1} \sum_{A_2} y_C y_{A_1} y_{A_2} L_{(C)(A_1, A_2)}^{\text{liq}} + \sum_C \sum_A y_C y_A y_{Va} L_{(C)(A, Va)}^{\text{liq}} \\ & + \sum_C \sum_A \sum_B y_C y_A y_B L_{(C)(A, B)}^{\text{liq}} + \sum_C \sum_B y_C y_B y_{Va} L_{(C)(B, Va)}^{\text{liq}} \\ & + \sum_{B_1} \sum_{B_2} y_{B_1} y_{B_2} L_{(B_1, B_2)}^{\text{liq}} \end{aligned} \quad (7)$$

The interactions between the different species on each sublattice are represented by the L parameters. When several species are interacting in the same sublattice, a coma is used to separate them. The parameters of the model are detailed in the next section for both Pu–O and U–Pu–O

systems.

3.1.1. Pu–O system

The two-sublattice model

$$(Pu^{3+})_p(O^{2-}, Va^{0-}, O, PuO_2)_q \quad (8)$$

is adopted to describe the liquid phase in the Pu–O system, with P and Q coefficients equal to

$$P = 2y_{O^{2-}} + Qy_{Va^{0-}} \text{ and } Q = 3 \quad (9)$$

According to equation (4), the Gibbs energy of the liquid phase G^{liq} is

$$\begin{aligned} G^{liq} = & y_{O^{2-}} {}^0G_{(Pu^{3+})(O^{2-})}^{liq} + Qy_{Va^{0-}} {}^0G_{Pu}^{liq} \\ & + Qy_{PuO_2} {}^0G_{PuO_2}^{liq} + Qy_O {}^0G_O^{liq} \\ & + RT [Q(y_{O^{2-}} \ln y_{O^{2-}} + y_{Va^{0-}} \ln y_{Va^{0-}} + y_{PuO_2} \ln y_{PuO_2} + y_O \ln y_O)] \quad (10) \\ & + y_{O^{2-}} y_{Va^{0-}} \left[{}^0L_{(Pu^{3+})(O^{2-}, Va^{0-})} + (y_{O^{2-}} - y_{Va^{0-}})^1 L_{(Pu^{3+})(O^{2-}, Va^{0-})} \right] \\ & + y_{O^{2-}} y_{PuO_2} {}^0L_{(Pu^{3+})(O^{2-}, PuO_2)} \end{aligned}$$

The $L_{(Pu^{3+})(O^{2-}, Va^{0-})}$ interaction parameters describe the liquid phase in the Pu–Pu₂O₃ region whereas $L_{(Pu^{3+})(O^{2-}, PuO_2)}$ is used to model the Pu₂O₃–PuO₂ composition range.

3.1.2. U–Pu–O system

The liquid phase of the ternary U–Pu–O is described using the extended two-sublattice model

$$(Pu^{3+}, U^{4+})_p(O^{2-}, Va^{0-}, O, PuO_2)_q \quad (11)$$

A schematic representation of the model is presented in Fig. 2, where the interactions between the different species to describe the ternary liquid phase are shown.

The Gibbs energy function for the liquid phase is

$$\begin{aligned} G^{liq} = & y_{O^{2-}} {}^0G_{(Pu^{3+})(O^{2-})}^{liq} + y_{U^{4+}} y_{O^{2-}} {}^0G_{(U^{4+})(O^{2-})}^{liq} + Qy_{Va^{0-}} {}^0G_{Pu}^{liq} + Qy_{Va^{0-}} {}^0G_U^{liq} \\ & + Qy_{PuO_2} {}^0G_{PuO_2}^{liq} + Qy_O {}^0G_O^{liq} + RT [P(y_{Pu^{3+}} \ln y_{Pu^{3+}} + y_{U^{4+}} \ln y_{U^{4+}}) \\ & + Q(y_{O^{2-}} \ln y_{O^{2-}} + y_{Va^{0-}} \ln y_{Va^{0-}} + y_{PuO_2} \ln y_{PuO_2} + y_O \ln y_O)] \\ & + y_{Pu^{3+}} y_{O^{2-}} y_{Va^{0-}} \left[{}^0L_{(Pu^{3+})(O^{2-}, Va^{0-})} + (y_{O^{2-}} - y_{Va^{0-}})^1 L_{(Pu^{3+})(O^{2-}, Va^{0-})} \right] \\ & + y_{Pu^{3+}} y_{O^{2-}} y_{PuO_2} {}^0L_{(Pu^{3+})(O^{2-}, PuO_2)} + y_{U^{4+}} y_{O^{2-}} y_{Va^{0-}} \left[{}^0L_{(U^{4+})(O^{2-}, Va^{0-})} \right. \\ & \left. + (y_{O^{2-}} - y_{Va^{0-}})^1 L_{(U^{4+})(O^{2-}, Va^{0-})} + (y_{O^{2-}} - y_{Va^{0-}})^2 L_{(U^{4+})(O^{2-}, Va^{0-})} \right] \\ & + y_{U^{4+}} y_{O^{2-}} y_O {}^0L_{(U^{4+})(O^{2-}, O)} + y_{Pu^{3+}} y_{U^{4+}} y_{Va^{0-}} \left[{}^0L_{(Pu^{3+}, U^{4+})(Va^{0-})} \right. \\ & \left. + y_{Va^{0-}} {}^1L_{(Pu^{3+}, U^{4+})(Va^{0-})} \right] + y_{Pu^{3+}} y_{U^{4+}} y_{O^{2-}} y_{Va^{0-}} {}^0L_{(Pu^{3+}, U^{4+})(O^{2-}, Va^{0-})} \\ & + y_{U^{4+}} y_{O^{2-}} y_{PuO_2} \left[{}^0L_{(U^{4+})(O^{2-}, PuO_2)} + (y_{O^{2-}} - y_{PuO_2})^1 L_{(U^{4+})(O^{2-}, PuO_2)} \right] \quad (12) \end{aligned}$$

In addition to the interaction parameters in the binary U–O, Pu–O [7] and U–Pu [30] sub-systems, the following ternary parameters have been introduced to describe the ternary system:

- The ${}^nL_{(U^{4+})(O^{2-}, PuO_2)}$ parameters to describe the solidus/liquidus temperatures along the UO₂–PuO₂ composition line;
- The ${}^0L_{(Pu^{3+}, U^{4+})(O^{2-}, Va^{0-})}$ parameter to improve the description of the melting temperatures of mixed oxides in the hypo-stoichiometric range ($O/M < 2.00$).

3.2. Results

The modified models for both the Pu–O and U–Pu–O systems will be described here and a comparison with the experimental data will be presented.

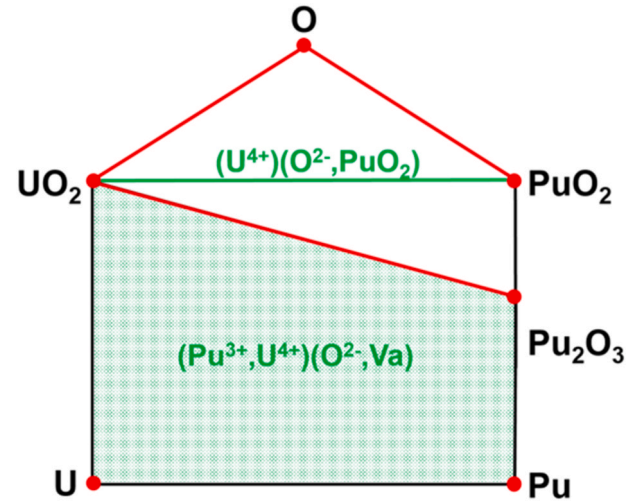


Fig. 2. Schematic representation of the model of the liquid phase for the U–Pu–O system.

3.2.1. Pu–O system

In 2008, Guéneau et al. published a first CALPHAD model of the Pu–O system [32] based on the critical analysis of the experimental data performed by H.A. Wriedt [33]. This version was revised in 2011 [3], to improve the description of the miscibility gap in the fluorite PuO_{2-x} phase and to take into account the melting temperature of PuO₂ (3017 ± 28 K) measured by De Bruycker et al. in 2010 [16]. Only the parameters of the liquid phase are modified in the present work.

The Gibbs energy function of the liquid phase is described by Equation (10).

In a first step, the melting enthalpy ΔH_{melt} and entropy ΔS_{melt} in the Gibbs energy function for the two end-members, pure liquid Pu₂O₃ (${}^0G_{(Pu^{3+})(O^{2-})}^{liq} = G_{Pu_2O_3} + \Delta H_{melt} + T\Delta S_{melt}$) and pure liquid PuO₂ (${}^0G_{PuO_2}^{liq} = G_{PuO_2} + \Delta H_{melt} + T\Delta S_{melt}$), were slightly modified. The values recommended for melting of Pu₂O₃ and PuO₂ by Konings et al. were used [14]. The entropies of melting were then adjusted to reproduce the selected melting points for the two compounds [5,14] (see section 2.1).

In a second step, the Pu₂O₃–PuO₂ solidus and liquidus curves were modelled by adjusting the interaction parameter between both end-members ${}^0L_{(Pu^{3+})(O^{2-}, PuO_2)}$ to reproduce the melting temperature measured by Böhler et al. [5]. With this model, a shift of the congruent melting to lower O/Pu ratios is observed, due to the high oxygen potential of PuO_{2-x} and its ability to lose oxygen above 2000 K. The new parameters are reported in Table 4 (Appendix). The calculated phase diagram is presented in Fig. 3(a) and a comparison with the experimental data is shown in Fig. 3(b).

With the updated parameters, the melting behaviour is well reproduced in the Pu₂O₃–PuO₂ region. Indeed, the melting point of Pu₂O₃ is calculated at 2350 K in agreement with the data of Chikalla (2360 ± 20 K) [17] and the recommendation of Konings et al. (2352 ± 10 K) [14]. The eutectic reaction (Liquid → Pu₂O₃ + PuO_{2-x}) temperature is found at 2325 K in agreement with the experimental data of Chikalla (2303 K). The calculated solidus and liquidus curves are also in good agreement with the experimental data for O/Pu = 1.62 and 1.65 measured by Chikalla et al. [17]. The dioxide is found to melt congruently at 3042 K for O/Pu = 1.95 (compared to 3000 K for O/Pu = 1.96 in Ref. [32]), in agreement with the data of Böhler et al. (3050 ± 59 K) [5]. The calculated invariant reaction (Liquid → PuO_{2-x} + O₂(g)) occurs at 3015 K, but no experimental data exist for comparison.

This model does not reproduce the melting temperature measured by Kato for PuO_{1.76}. However, in the measurements performed by Kato et al. [19] and Böhler et al. [5], the O/Pu ratio in the samples is

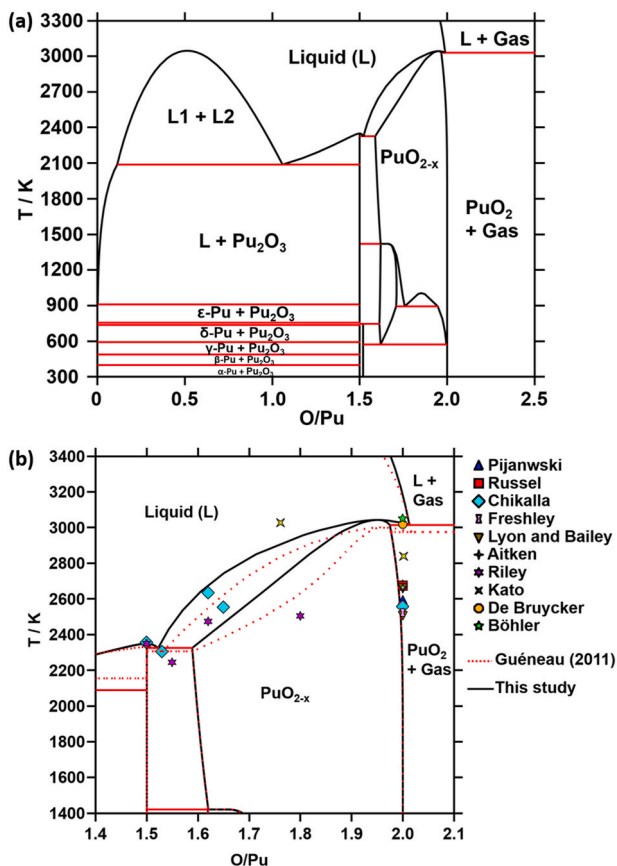


Fig. 3. (a) Calculated phase diagram of the Pu–O system as a function of the O/Pu ratio and (b) Zoom on the 1.4 < O/Pu < 2.2 composition range.

unknown. Furthermore, a change in the composition due to incongruent sublimation in the Pu–O system could have occurred in both cases [34]. Thus, the liquidus and solidus curves between Pu₂O₃ and PuO₂ remain uncertain and further measurements are needed to improve this present model.

3.2.2. U–Pu–O system

The Gibbs energy parameters of the model of Guéneau et al. [7] were used as a starting point in this study. In a first step, the modified

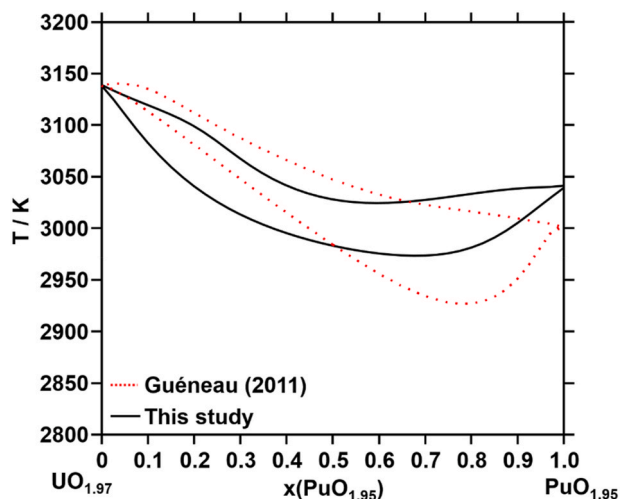


Fig. 4. Calculated UO_{1.97}–PuO_{1.95} phase diagram compared to Guéneau et al. (dashed line) [7].

parameters for the Pu–O liquid phase previously described were introduced in the model. In a second step, the ternary interaction parameters of the liquid were reassessed to better reproduce the data selected in section 2.

The interaction parameters ${}^0L_{(U^{4+})(O^{2-},PuO_2)}$ and ${}^1L_{(U^{4+})(O^{2-},PuO_2)}$, describing the UO₂–PuO₂ composition line, were first modified to fit the selected experimental data for U_{1-y}Pu_yO_{2.00} samples of Böhler et al. [5] for y > 0.5 and Kato et al. for y < 0.5 [5,19] (see section 2.2). The calculated isopleth section between UO_{1.97} and PuO_{1.95} (corresponding to the congruent melting compositions for U–O and Pu–O) is presented in Fig. 4 with the previous model of Guéneau et al. (dashed line) [7]. Both solidus and liquidus curves are shifted towards lower temperature in the U-rich region whereas, on the contrary, the calculated temperatures are higher in the Pu-rich zone. Fig. 5 illustrates the comparison between the calculations and the selected experimental data. Overall, a very good agreement is obtained with the data of Kato et al. [23] and Böhler et al. [5]. Moreover, in agreement with De Bruycker et al. [8] and Böhler et al. [5], a minimum in the solidus temperature is observed around y = 0.7.

To describe the hypo-stoichiometric region, the interaction parameters, namely ${}^0L_{(Pu^{3+},U^{4+})(O^{2-})}$ and ${}^0L_{(Pu^{3+},U^{4+})(O^{2-},PuO_2)}$, used in the model of Guéneau et al. of 2011, were removed and replaced by a single interaction parameter: ${}^0L_{(Pu^{3+},U^{4+})(O^{2-},Va^{2-})}$. This parameter, stabilizing the liquid phase towards the metallic liquid. It was assessed to describe the solidus/liquidus data of Kato measured in the hypostoichiometric region (1.925 < O/M < 2) for y = 0.118, 0.199 and 0.397 [23].

The new thermodynamic parameters for the liquid are reported in Table 5 (Appendix).

The calculated isopleth sections for y = 0.12, 0.20 and 0.40 are compared with the selected data of Kato in Fig. 6 (a), (b), (c) respectively. A good agreement is found within the experimental uncertainties (respectively ± 35 K and ± 50 K for the solidus and liquidus temperatures). However, the model tends to systematically underestimate the solidus temperatures in the near-stoichiometry region. Moreover, large uncertainties remain on the experimental data, in particular on the exact O/M ratio of the samples, as no detailed information nor uncertainties are given by the authors.

Calculated isothermal sections of the U–Pu–O system at 1500, 2500 and 3000 K are shown in Fig. 7. It can be noticed that the tie lines (in green), giving the compositions of the two phase region (U_{1-y}Pu_yO_{2±x} + Liquid), do not lie along the UO₂–PuO₂ composition line. Thus, the UO₂–PuO₂ system is not a pseudo-binary system and the simplified ideal model described by Carbajo et al. is considered as not reliable [11]. The

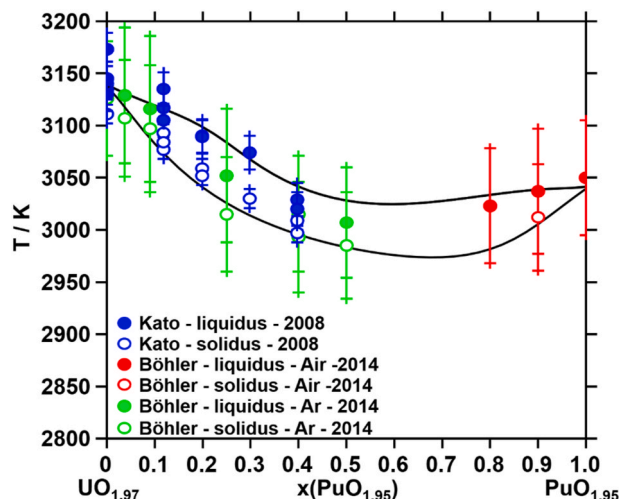


Fig. 5. UO_{1.97}–PuO_{1.95} phase diagram compared with the selected experimental data of Kato et al. [19] and Böhler et al. [5].

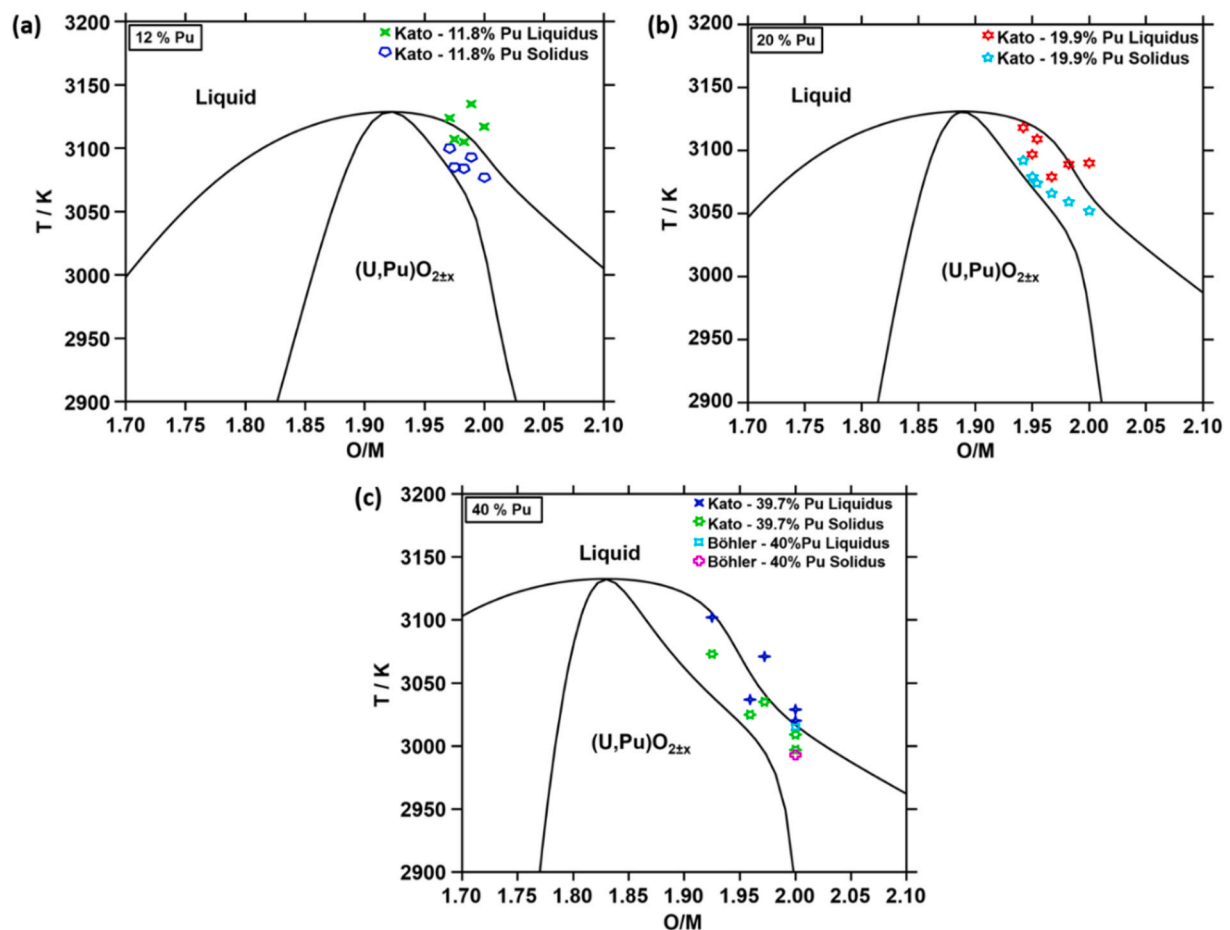


Fig. 6. Calculated isopleths sections of the U-Pu-O diagram for $y =$ (a) 0.12, (b) 0.20 and (c) 0.40, compared to the selected experimental data of Kato [23] and Böhrler et al. [5]. The experimental uncertainties (± 30 K) are not represented here for clarity.

benefit of a CALPHAD model to provide an accurate description of the solidus/liquidus surface in the U-Pu-O system is highlighted here.

Moreover, the isothermal sections illustrate the complex melting behaviour in the metal-oxide region. Indeed, at 2500 and 3000 K, a biphasic domain with two oxide and metallic liquid phases, is highlighted. It arises from the existing miscibility gap above $T = 2088$ K in the Pu-O binary system [7]. The miscibility gap, appearing first in Pu-O, is then shifted towards high uranium contents when increasing the temperature. However, care should be taken when considering this composition range of the phase diagram, as no experimental data are available.

This re-assessment presents some limitations due to the lack of experimental data, particularly in the high plutonium content range. Moreover, no measurement was performed in the hyper-stoichiometric range, for which the model is only tentative. Further investigations are also needed in low oxygen stoichiometry range ($O/M < 1.90$) to better localise and model the maximum in the melting temperature. Moreover, as no *in-situ* experiments were performed during the melting tests, the exact oxygen stoichiometry at which the phase transitions were measured remains unknown. Thus, uncertainties linger in broad areas of the system and the model can be considered valid from $0 < y < 0.50$ and for O/M ratios between 1.90 and 2.00. Outside this range, this re-evaluation constitutes only a preliminary re-assessment.

To overcome this lack of data and try to determine the O/M ratio change of the fuels during melting, experimental investigations on post-melting samples were performed by means of XANES. The procedure and findings will be presented in the following section.

4. Determination of the sample composition after the laser heating tests

The melting temperatures of four $U_{1-y}Pu_yO_{2.00}$ samples $y = 0.14, 0.46, 0.55$ and 0.62 were measured by Strach et al. using laser heating under air and under argon as described in Ref. [9]. For the manufacturing of these samples, UO_2 and PuO_2 powders were mixed in various proportions to obtain the targeted Pu content, grinded and pressed into pellets. A sintering step of 24h at $1700^\circ C$ under a mixture of Ar/H_2 5% + z ppm H_2O was performed, with z the required amount of H_2O to obtain stoichiometric mixed oxides. Further details about the preparation of these samples can be found in Refs. [9,35].

Post-melting characterisations using X-ray Absorption Spectroscopy were performed on these samples and are presented here, where the samples are referred to as MOX_y-atm (example: MOX14-Air for $U_{0.86}Pu_{0.14}O_{2-x}$ melted under air). The aim is to determine the changes in the oxygen stoichiometry of the samples due to the laser melting tests performed at JRC Karlsruhe [9].

Although the solidus and liquidus temperatures obtained by Strach et al. [9] were not considered because of the lack of detailed information about the melting conditions in Ref. [9], the XAS results obtained were used in this work only for comparison with the modelling predictions and not for the re-assessment.

4.1. XANES method

The molten part of the samples was extracted from the rest of the molten disk of pellet, from which a small amount of powder was collected at JRC Karlsruhe. The powder was then mixed with boron

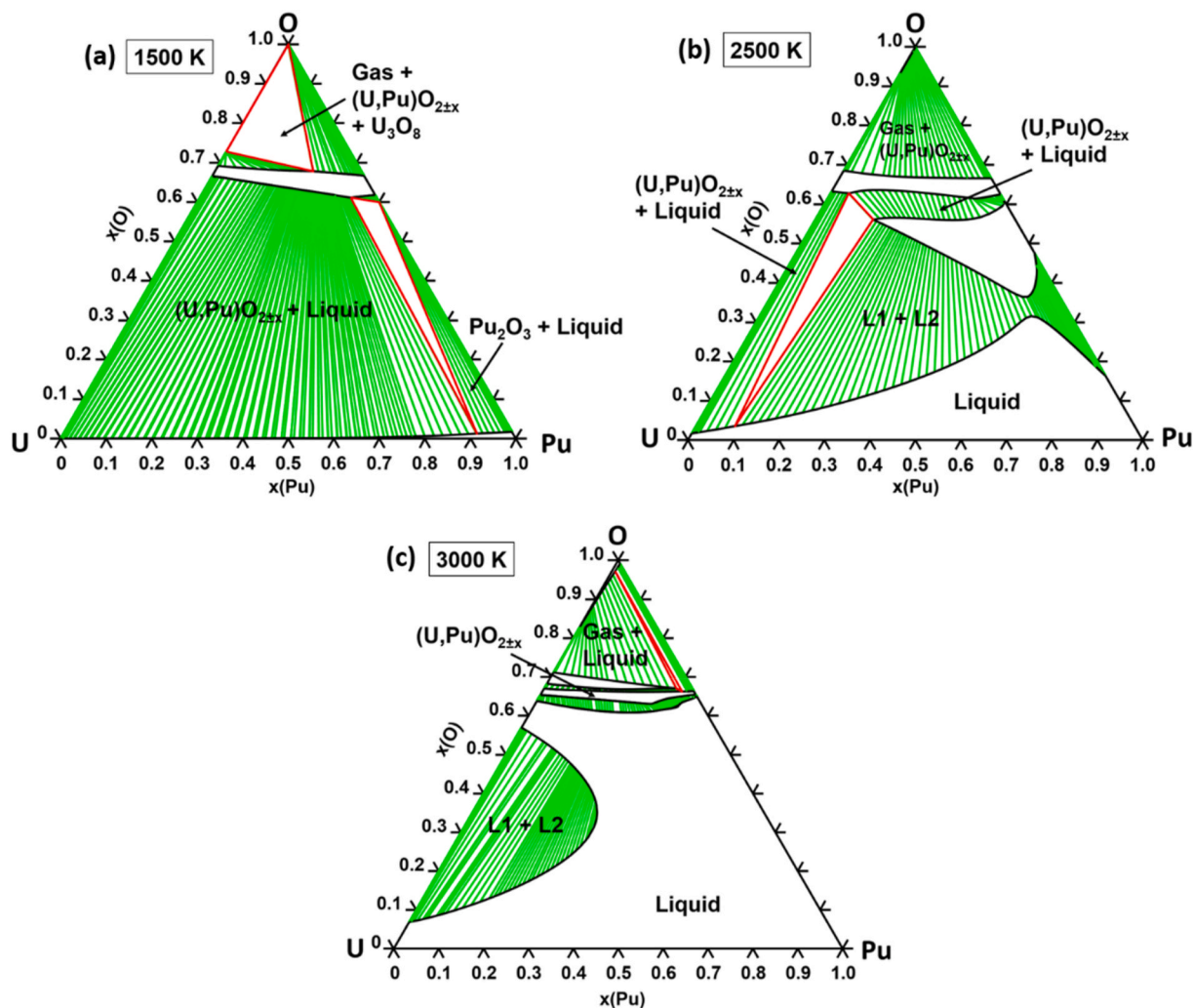


Fig. 7. Calculated isothermal sections at (a) 1500 K (b) 2500 K and (c) 3000 K of the U-Pu-O system.

nitride and pressed into pellets. Polyethylene sample holders (double confinement) were used to contain the samples. The measurements were performed at the INE beamline [36] at the KIT Light Source (KARA storage ring, Karlsruhe, Germany), under dedicated operating conditions (2.5 GeV, 120–150 mA) at room temperature. Spectra were collected at the U-L₃ (17166 eV) and Pu-L₃ (18057 eV) edges, with an interval of 400 eV centred on the nominal edge and a step of 0.8 eV. Transmission mode was used to acquire the spectra, thanks to argon-filled ionisation chambers. A Ge(422) double crystal monochromator coupled with collimating and focusing Rh-coated mirrors were used for energy selection. Metallic foils with K edges close to the edges of interest, yttrium (17038 eV) and zirconium (17998 eV), were employed for calibration. The references were placed between the second and third ionisation chambers and measured at the same time as the samples, in transmission mode. From 3 to 6 spectra were acquired for each sample and edge to improve statistical sampling.

The X-ray Absorption Near Edge Structure (XANES) data were analysed using the Athena Software [37]. The normalisation of the spectra was performed using a linear function for pre-edge and post-edge signals. The white line inflection point (E_0) was determined by the use of first zero crossings of the second derivatives. The average oxidation states of the cations were determined by fitting the XANES data by linear combination of reference spectra. Fits were performed in the $E_0 - 30 \text{ eV} \leq E \leq E_0 + 30 \text{ eV}$ range. U^{+4}O_2 , $(\text{U}^{+5.2/3}, \text{U}^{+6.1/3})_3\text{O}_8$ and $(\text{U}^{+4.5}, \text{U}^{+5.5})_4\text{O}_9$ [38] were used as reference for the U-L₃ edge, as well as Pu^{+4}O_2 and $\text{Pu}^{+3}\text{PO}_4$ [39] for the Pu-L₃ edge.

4.2. Results

The XANES spectra collected on the melted samples under air and Ar are presented in Fig. 8, respectively for the U-L₃ and Pu-L₃ edges. The starting materials (before melting) were manufactured by Strach et al. and found to be stoichiometric ($\text{O}/\text{M} = 2.00$), i.e. containing only U^{+4} and Pu^{+4} [9].

For the spectra collected at the U-L₃ edge shown in Fig. 8 (a) and (b), a shift of the white line (WL) towards higher energies was observed, compared to the position of the UO_2 reference, for the two atmospheres studied in this work. This indicates an increase in the oxidation state of uranium. In the case of samples molten under Ar, this difference in WL position ranges between +0.05 eV for MOX14-Ar and +0.45 eV for MOX62-Ar. For the samples molten under air, a higher gap is observed with +1.89 eV for MOX14-Air, indicating a higher O/U ratio. The spectra of these samples molten under air are more similar to UO_2 and U_4O_9 than to U_3O_8 .

On the spectra at the Pu-L₃ edge of the MOX14-Air and MOX14-Ar samples, both WL inflection point and maxima are similar to the PuO_2 reference, indicating that plutonium remained purely tetravalent. For samples with $y > 0.14$, a shift of the WL towards lower energy is observed, indicating the reduction of the plutonium. Only a slight displacement of the WL maxima of a few tenths of electronvolts was noticed in case of melting under air, whereas under argon a more significant shift of the WL from the PuO_2 inflection point was observed and increased with Pu content.

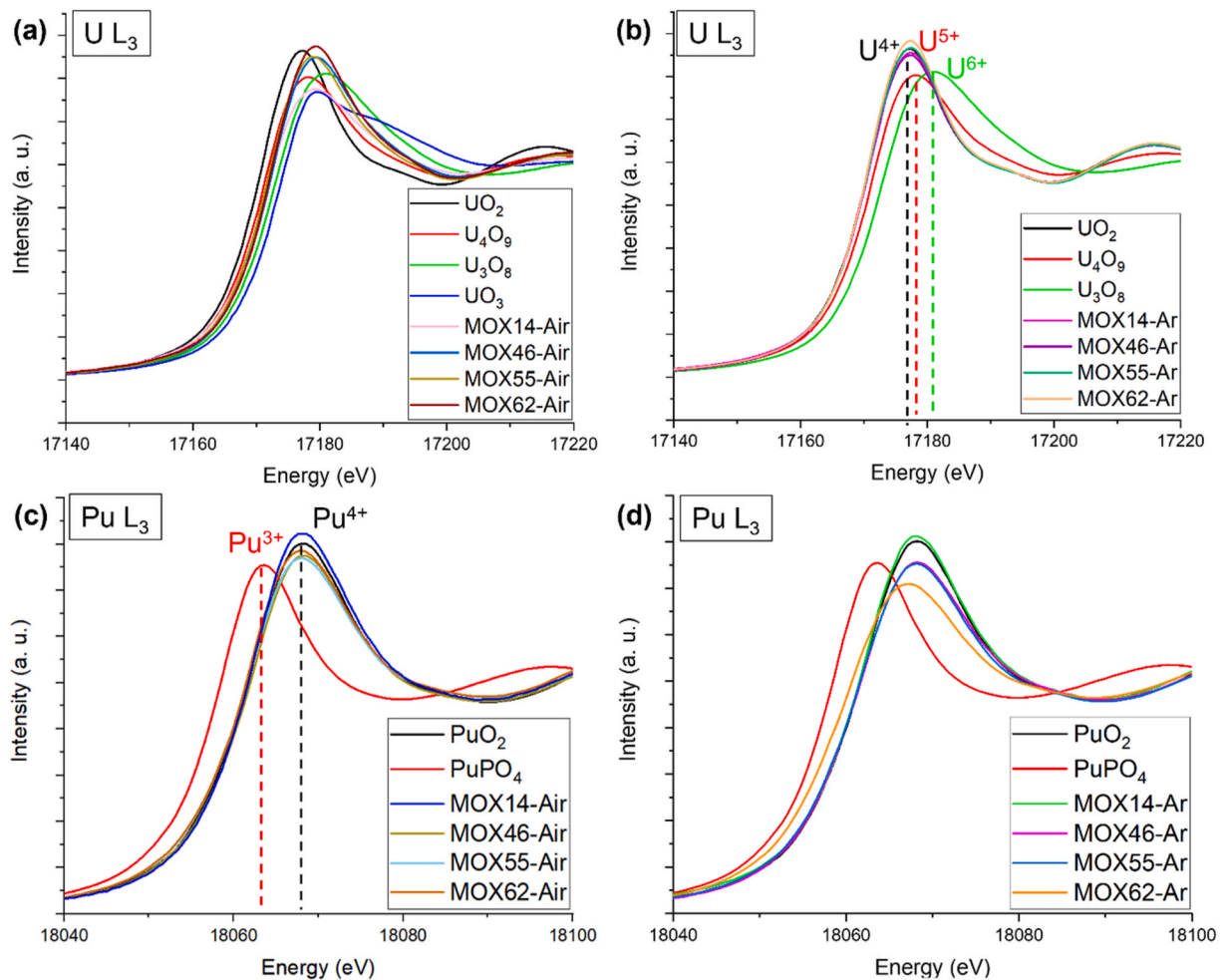


Fig. 8. XANES spectra collected at (a), (b) U-L₃ and (c), (d) Pu-L₃ edges for the melted samples under air ((a) and (c)) and Ar ((b) and (d)).

The oxidation states of the samples, determined by linear fitting of the reference spectra, as well as the resulting O/M ratios, are summarised in Table 2.

The oxidation state of uranium was found to be a mixture of +4, +5 and +6 in the samples molten under air, as can be seen in Table 2. In the case of melting under argon, uranium remains mainly tetravalent, although a small fraction of pentavalent uranium was noticed in the sample. No hexavalent uranium was observed for these samples.

In the case of plutonium, as previously stated, only tetravalent plutonium Pu⁴⁺ is observed in the MOX14-Air and MOX14-Ar samples. However, when increasing Pu content, an increase in the proportion of trivalent plutonium is observed. For samples molten under air, this contribution remains low, as air exhibits a tendency to oxidise the material at high Pu content. However, in the case of argon, the proportion of Pu³⁺ is increasing when increasing the plutonium content, from 7.5% for MOX46-Ar to 38.1% for MOX62-Ar. This observation is consistent with the fact that argon is a reducing atmosphere for materials with high Pu content.

The co-existence of U⁴⁺, U⁵⁺, U⁶⁺, Pu⁴⁺ and Pu³⁺ is observed in this work for the first time for U_{1-y}Pu_yO_{2±x} samples. This behaviour is noticed even for hyper-stoichiometric and near stoichiometric samples. It is contradictory to what is expected, as the plutonium is found only in its tetravalent form for O/M > 2.00. This observation indicates that partial charge compensation mechanisms are occurring in the samples. Prieur et al. already observed this phenomenon for U_{1-z}Am_zO_{2-x} samples of similar fluorite structure [40,41]. The slight hyper-stoichiometry observed for MOX14-Ar can be linked here to the instrumental uncertainty (±0.02).

Thus, contrarily to what was reported by Böhler et al. [5], where the post-melting composition of strongly oxidised samples was not measured, changes in the O/M ratio occur during the melting. Indeed, as it can be seen in Table 2, the molten materials all exhibit an O/M ratio different from the initial one (O/M = 2.00).

For samples melted under air, a significant increase in the oxygen stoichiometry was noticed, with O/M ratios higher than 2.00. These high O/M ratios indicate the formation of hyper-stoichiometric oxides, such as M₃O₈ and M₄O₉. This oxidation of the samples explains the decrease of the melting temperature under air, driven by the preferential oxidation of uranium. The non-reproducibility of the solidus temperatures reported under air (see green circles in Fig. 1) can be explained by the progressive oxidation of the samples occurring during the successive shots. The opposite behaviour was observed for samples melted under argon. Except for MOX14-Ar, all the samples are hypo-stoichiometric. The effect of the atmosphere on melting behaviour will be discussed in the next section.

5. Discussion on the melting behaviour of U_{1-y}Pu_yO_{2±x} mixed oxides

In this section, the influence of the plutonium and oxygen content on the melting behaviour of U_{1-y}Pu_yO_{2±x} mixed oxides will be first discussed based on the reassessment of the U-Pu-O model performed in this work. Then, calculations results reproducing the experimental conditions of the laser heating melting and studying the influence of the atmosphere during the measurements will be discussed. Finally, computed solidification paths will be presented to understand the

Table 2

Average oxidation states of uranium (U^{+z} , with $z = 4, 5$ or 6) and plutonium (Pu^{+z} , with $z = 3$ or 4) and corresponding O/M ratio after melting for MOXy-Atm. The sum of the cations is equal to 1 for each element and the uncertainty on the cationic proportion is equal to $\pm 5\%$. The O/M ratio before melting and the solidus temperatures measured by Strach et al. are also indicated [9].

Sample	y(Pu)	$U^{+z} \pm 5\% (\Sigma = 1)$			O/U	$Pu^{+z} \pm 5\% (\Sigma = 1)$		O/Pu
		U^{+4}	U^{+5}	U^{+6}		Pu^{+4}	Pu^{+3}	
MOX14-Air	0.14	32	56	12	2.40	100	0	2.00
MOX14-Ar	0.14	94	6	0	2.03	100	0	2.00
MOX46-Air	0.46	25	58	17	2.46	99	1	2.00
MOX46-Ar	0.46	96	4	0	2.02	93	7	1.96
MOX55-Air	0.54	38	54	8	2.35	92	8	1.96
MOX55-Ar	0.54	99	1	0	2.01	90	10	1.95
MOX62-Air	0.62	30	56	14	2.42	94	6	1.97
MOX62-Ar	0.62	99	1	0	2.00	62	38	1.81

Sample	O/M before melting [9]	O/M after melting (± 0.02)	Solidus temperature ± 50 K [9]
MOX14-Air	2.00	2.34	2900
MOX14-Ar	2.00	2.02	3065
MOX46-Air	2.00	2.25	2875
MOX46-Ar	2.00	1.99	2970
MOX55-Air	2.00	2.14	2930
MOX55-Ar	2.00	1.97	2995
MOX62-Air	2.00	2.14	2920
MOX62-Ar	2.00	1.88	2940

change in oxygen stoichiometry occurring during the cooling of the samples.

5.1. Influence of the Pu content and O/M ratio

Calculated 3D maps of the solidus (in blue) and liquidus (in green) temperatures of the U–Pu–O system as a function of temperature, Pu content and O/M ratio are shown Fig. 9. These calculations were performed using a Python script developed using the TC-Python software.

To understand the melting behaviour of the ternary system U–Pu–O, the binary systems U–O (Fig. 9 (a)) and Pu–O (Fig. 9 (b)) have to be investigated first. In the U–O system, the congruent melting point (where the composition of liquid is equal to the one of the solid) is calculated at 3139 K for a slightly hypo-stoichiometric dioxide (O/M = 1.98) [7]. As observed in Fig. 9 (a), from this maximum, the solidus and liquidus temperatures decrease towards both the hypo- and hyper-stoichiometric regions. For the Pu–O system, at high temperature, PuO_2 tends to lose oxygen above 2100 K. This results in a shift of the

congruent melting composition, determined at 3042 K, to a slightly lower O/M = 1.95 (see Fig. 3(b)).

For the U–Pu–O system, the melting temperature and the O/M ratio at the congruent melting are plotted in Fig. 10 (a) and (b), respectively.

On Fig. 10(a), starting from $UO_{1.98}$, the congruent melting temperature is nearly constant in the 3130–3140 K range up to $U_{0.55}Pu_{0.45}O_{1.82}$, where it decreases when increasing the Pu content up to 3042 K for $PuO_{1.95}$. A maximum in the melting temperature was found at 3134 K for $U_{0.67}Pu_{0.33}O_{1.85}$. As it can be seen in Fig. 10(b), the O/M ratio at congruency follows a “V” shape: it decreases when Pu content increases to a minimum value of 1.797 for $y = 0.6$, and then increases for higher Pu contents (Fig. 10(b)). This line represents the summit of the 3D maps represented in Fig. 9 (a) and (b) and a decrease of both the solidus and liquidus temperatures is noticed from this peak when increasing or lowering the O/M ratio.

These calculations clearly show that the oxygen stoichiometry and the Pu content have significant influences on the melting behaviour of the uranium-plutonium mixed dioxides. As also shown in the calculated

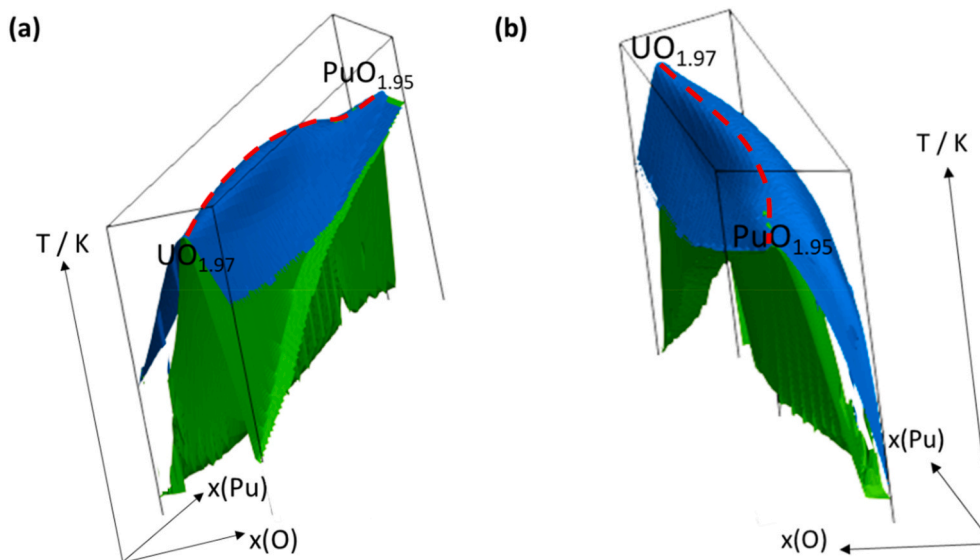


Fig. 9. 3D map of the liquidus (in blue) and solidus (in green) temperatures in the U–Pu–O system, (a) from the UO_{2-x} side and (b) the PuO_{2-x} side. The dashed red lines correspond to the congruent melting composition. The boundaries of the 3D maps are $0.61 < x(O) \leq 0.69$, $0 < x(Pu) \leq 1$ and $2500 < T \leq 3200$ K.

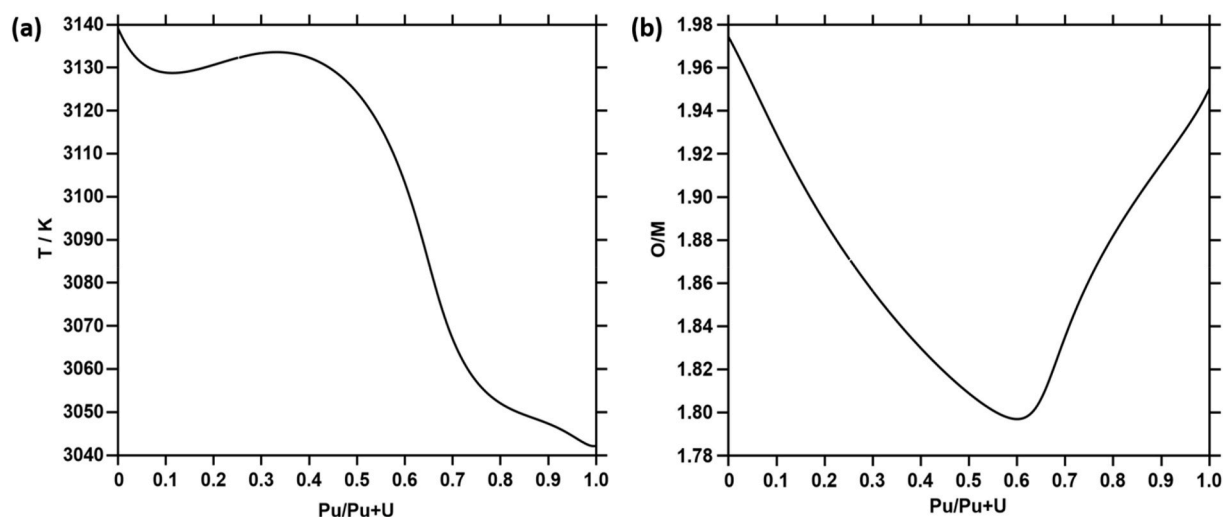


Fig. 10. (a) Temperature and (b) O/M ratio at the congruency as a function of the Pu content in $U_{1-y}Pu_yO_{2-x}$.

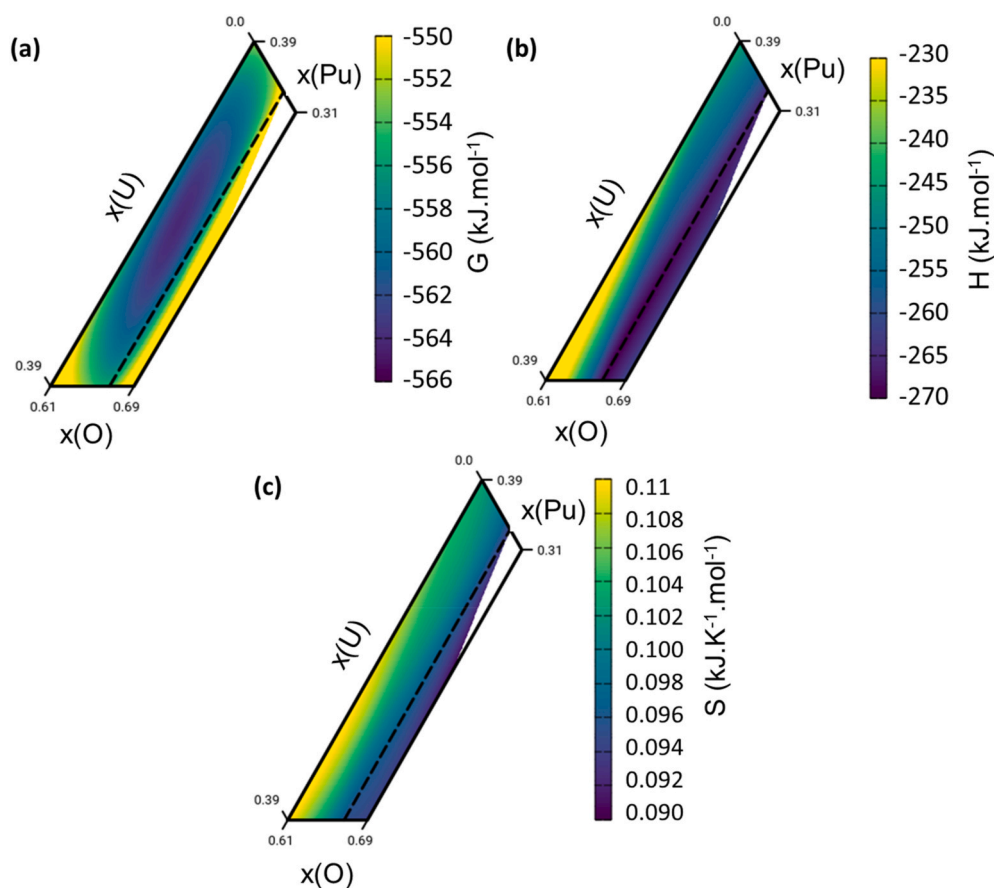


Fig. 11. Maps of (a) the Gibbs energy, (b) the enthalpy, (c) the entropy of $U_{1-y}Pu_yO_{2\pm x}$ mixed oxide as a function of the composition in mole fraction at 3000 K.

isopleth sections on Fig. 6, for a fixed Pu content ranging between 0.12 and 0.40, the solidus and liquidus temperatures increase from $O/M = 2.00$ to a maximum located around 1.8–1.9.

To understand the origin of this shift of the congruency towards the hypo-stoichiometric region, the stability of the mixed oxides was investigated as a function of the Pu content and O/M ratio.

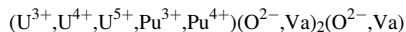
Using the model proposed in this work, a map of the Gibbs energy at 3000 K of $U_{1-y}Pu_yO_{2\pm x}$ is plotted in Fig. 11(a). The existence of a minimum for $U_{0.55}Pu_{0.45}O_{1.82}$ can be observed, away from stoichiometry

(indicated by the dashed line). This observation shows that, at high temperature, the mixed oxide is stabilised in the hypo-stoichiometric region. This could explain the location of the highest melting temperature in this O/M range.

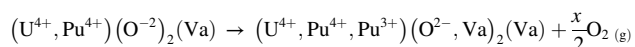
Maps for the enthalpy and entropy of configuration of $U_{1-y}Pu_yO_{2\pm x}$ calculated at 3000 K are shown in Fig. 11(b) and (c). Regardless of the Pu content, the enthalpy of the mixed oxide shows a minimum for $O/M = 2.00$, from which it increases for both positive and negative deviations. On the contrary, the entropy follows a different trend, with a

continuous increase when decreasing the O/M ratio. It can be concluded that the minimum of the Gibbs energy observed for $U_{0.55}Pu_{0.45}O_{1.82}$ results in the combination of both enthalpic and entropic contributions. Moreover, the entropic contribution is predominant at 3000 K and can explain the stabilisation of the mixed oxide in the hypo-stoichiometric region.

In this work, based on the model of Guéneau et al. [7], the Gibbs energy of $U_{1-y}Pu_yO_{2\pm x}$ is described using the three-sublattice model



The first sublattice contains uranium and plutonium cations with different oxidation states. The second sublattice corresponds to the normal tetrahedral oxygen site. The third sublattice is the interstitial oxygen site. The occupation rate of both oxygen sites can vary thanks to the introduction of vacancies, denoted “Va”. Starting from an O/M ratio equal to 2, the reduction of the mixed oxides leads to the increase of the oxygen vacancy concentration in the second sublattice. To compensate this oxygen loss, because of the higher oxygen potential of PuO_2 compared to the one of UO_2 , the plutonium is first reduced from Pu^{4+} to Pu^{3+} according to reaction



Once all the Pu^{4+} is reduced into Pu^{3+} , for lower O/M ratio, uranium is then reduced from U^{4+} to U^{3+} . At high temperature, in stoichiometric UO_2 , a significant fraction of defects is observed, with U^{3+} and U^{5+} in the first sublattice, oxygen vacancies Va and interstitial oxygen in the second and third sublattices. Thus, the configurational entropy S of $U_{1-y}Pu_yO_{2\pm x}$ is the result of disorder on both metallic and oxygen sites and can be described as a sum of the following contributions:

$$\text{For plutonium : } S_{Pu} = -R (y_{Pu^{3+}} \ln y_{Pu^{3+}} + y_{Pu^{4+}} \ln y_{Pu^{4+}}) \quad (15)$$

$$\text{For uranium : } S_U = -R (y_{U^{3+}} \ln y_{U^{3+}} + y_{U^{4+}} \ln y_{U^{4+}} + y_{U^{5+}} \ln y_{U^{5+}}) \quad (16)$$

$$\text{For oxygen : } S_O = -R \left[\begin{array}{l} 2 (y_{Va} \ln y_{Va} + y_{O^{2-}} \ln y_{O^{2-}})_{normal\ O\ sublattice} \\ + (y_{Va} \ln y_{Va} + y_{O^{2-}} \ln y_{O^{2-}})_{interstitial\ O\ sublattice} \end{array} \right] \quad (17)$$

where R is the gas constant (equals to $8.314\ J\ mol^{-1}\ K^{-1}$) and y_i are the site fractions of the species occupying the different sublattices.

Thus, when decreasing the O/M ratio, the increase of both oxygen vacancies and Pu^{3+} fractions leads to the increase of the total configurational entropy, as shown in Fig. 11.

As an example, the configurational entropy for Pu, U, and O, as well as the total one, was calculated in Fig. 12. The dashed lines indicate the limit of stability of the solid phase at this temperature. A maximum in

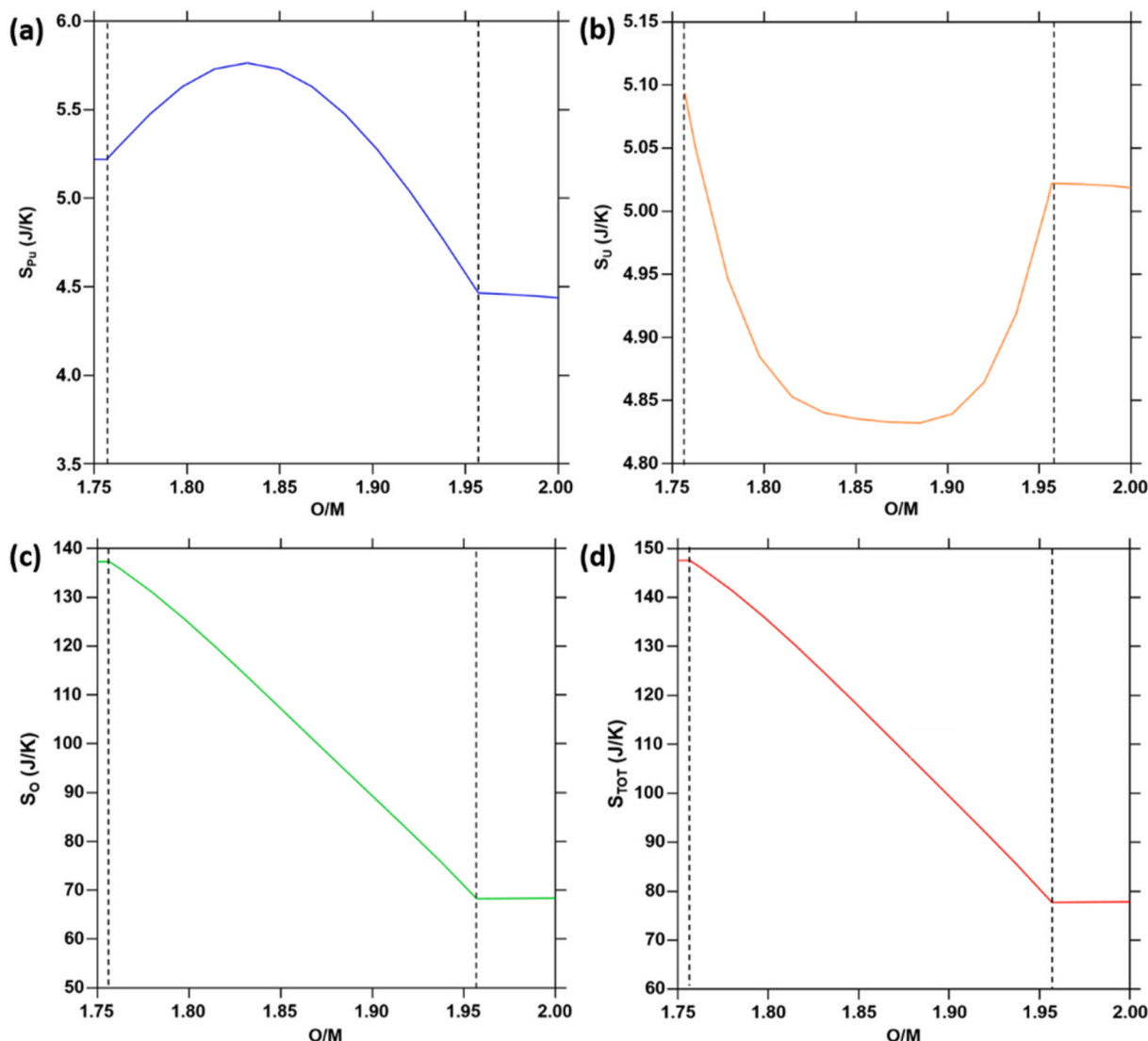


Fig. 12. Configurational entropy of (a) Pu, (b) U, (c) O and (d) total at 3000 K as a function of the O/M ratio for $y = 0.50$.

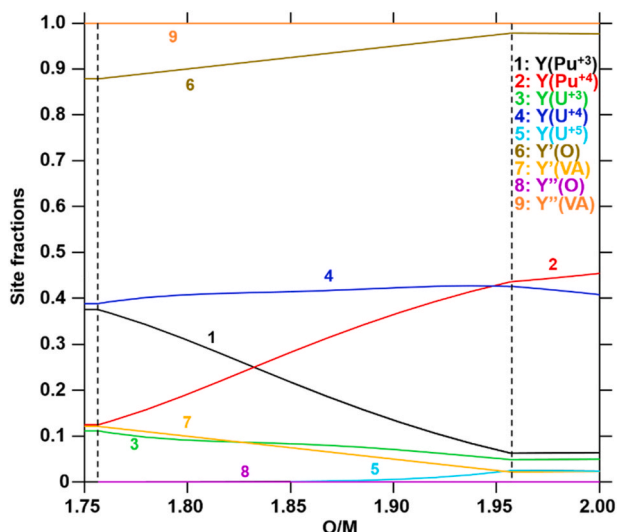


Fig. 13. Calculated site fractions at 3000 K as a function of the O/M ratio for $y = 0.50$.

the configurational entropy of Pu (Fig. 12(a)) is observed for $O/M = 1.84$, while a minimum is observed at this O/M ratio for the one of uranium (Fig. 12(b)). Moreover, the entropic contribution of the oxygen vacancy formation (Fig. 12(c)) appears to be predominant in the total configurational entropy (Fig. 12(d)).

For a better understanding, the site fractions of the different species are plotted for the same Pu content and temperature ($y = 0.50$ and 3000 K) as a function of the O/M ratio, as illustrated in Fig. 13. At $O/M = 1.84$, the site fractions of Pu^{3+} and Pu^{4+} are equal, which explains the maximum of the configurational entropy of Pu (Fig. 12(a)). Moreover, the site fraction of U^{4+} remains constant over the O/M range described here, in agreement with the reduction of Pu^{3+} first.

The simultaneous presence of U^{5+} , U^{4+} , Pu^{3+} and Pu^{4+} at 3000 K can be observed in Fig. 13 for $1.90 \leq O/M \leq 2.00$. This is in agreement with the site fractions already determined experimentally at 298 K in 4.2, except for U^{6+} which was also observed in samples molten under air. This indicates that the cations present at high temperatures correspond to those determined at low temperature, with only their proportions varying due to the reduction of the sample with temperature. A charge compensation mechanism is also supposed to occur at high temperature in the near-stoichiometric region. The presence of U^{6+} is not shown in

the calculations as it is not considered as a stable cation in the $U_{1-y}Pu_yO_{2\pm x}$ phase. The formation of M_3O_8 could explain its presence.

These calculations illustrate the stabilisation of $U_{1-y}Pu_yO_{2\pm x}$ with increasing Pu content and decreasing the O/M ratio. This trend is in agreement with the one observed for the congruent melting, *i.e.* when increasing Pu content, the congruent melting temperature is shifted towards lower O/M ratios (see Fig. 6). This observation is also in agreement with the study of Aitken and Evans [3], who explained the congruent melting by the stabilisation of the oxide and the formation of oxygen vacancies and Pu^{3+}/Pu^{4+} disorder.

In addition, the influence of the stability of the liquid phase on the melting temperature of the mixed oxide also has to be taken into account. However, as no thermodynamic data exist on the liquid phase, this influence could not be discussed in the present work.

5.2. Influence of the atmosphere

5.2.1. Argon or air

To represent in the most accurate way the experimental conditions of the laser heating measurements, calculations of the solidus temperatures of $U_{1-y}Pu_yO_{2\pm x}$ mixed oxides and O/M ratio as a function of the plutonium content were performed using the model of this work. These results are summarised in Fig. 14 (a) and (b), respectively. The thermodynamic equilibrium between the samples and the atmosphere was considered for two atmospheres: argon (green) or air (red) at a pressure of 0.3 MPa. For these calculations, 5 mol of gas were used as input, as well as 1 mol of metal (U + Pu) and 2 mol of oxygen.

Under air, a significant increase of the solidus temperature is noticed when increasing the plutonium content. On the contrary, under argon, a slight decrease occurs towards higher Pu contents, where a minimum is observed around $y = 0.50$. A good agreement is obtained with the experimental data available under air and argon for the calculated solidus temperatures. The results for the liquidus temperatures, not presented here, follow the same trend.

When looking at the variation of the O/M ratio as a function of Pu content in Fig. 14(b), the same trend is observed for the two atmospheres. In air, the uranium-rich samples are oxidised up to $y = 0.15$, where the reduction of the mixed oxides starts. The hyper-stoichiometry noticed for high uranium contents is explained by the tendency of UO_2 to oxidise into UO_{2+x} , whereas PuO_{2+x} is not stable. On the contrary, under argon, the mixed oxides are predicted to be all hypo-stoichiometric in oxygen, regardless of the plutonium content.

Thus, for uranium-rich compositions, argon is the most reliable

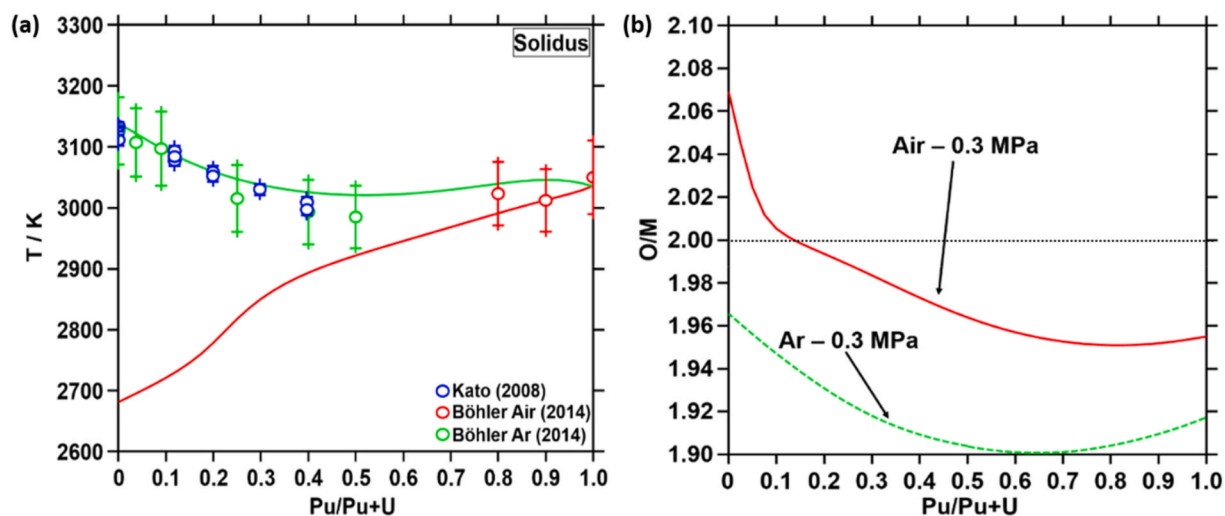


Fig. 14. Calculated (a) solidus temperatures compared to the experimental data of Kato et al. [19] and Böhler et al. [5] and (b) O/M ratio at the solidus temperature as a function of Pu content, under air in red and argon in green. The calculations were performed for 5 mol of gas and 3 mol of samples.

atmosphere to maintain an O/M ratio as close as possible to 2. On the contrary, air is more appropriate in case of plutonium-rich mixed oxides ($y > 0.50$) to avoid the loss of oxygen due to the high oxygen potential of PuO_2 , and thus to maintain the oxygen stoichiometry as close as possible to 2.00.

5.2.2. Number of moles of gas

The section proposes a determination of the number of moles of gas reacting with the samples and its effect on the solidus temperature and O/M ratio of the melting.

An estimation of the number of moles of gas reacting with the molten pool of the sample was proposed by Quaini et al. in their investigation of melting temperatures in the $\text{UO}_2\text{-PuO}_2\text{-ZrO}_2$ system by laser heating [42]. Considering a laminar gas flow, a ratio of 3/1 was determined between the numbers of moles of gas reacting with the sample within a boundary layer. Using the same approach, the following amounts of samples and gas were calculated in the present work:

- $1.8 \cdot 10^{-3}$ mol for the sample pellet of composition $\text{U}_{0.75}\text{Pu}_{0.25}\text{O}_2$ ($M = 271.5 \text{ g mol}^{-1}$, density = 10.5 g cm^{-3} , diameter = 8 mm, thickness = 1 mm);
- $1.1 \cdot 10^{-4}$ mol for the molten pool calculated from the volume of the molten pool equal to 3 mm^3 (diameter = 5 mm in (corresponding to the laser spot) and depth = $150 \text{ }\mu\text{m}$ [27]);
- $1.6 \cdot 10^{-1}$ mol of gas in the whole chamber (cylinder of 20 cm long and 10 cm diameter, filled with a gas of ideal behavior);
- $5.9 \cdot 10^{-6}$ mol of gas in the boundary layer. A laminar flow of buffer gas was assumed in the boundary layer, represented by a cylinder of 5 mm diameter and 3 mm thickness, from the surface of the molten pool.

The solidification paths of $\text{U}_{0.75}\text{Pu}_{0.25}\text{O}_2$ (T as a function of the O/M ratio) were calculated and are plotted in Fig. 15, considering a thermodynamic equilibrium with the gas phase. For these calculations, 1.1×10^{-4} mol of sample was assumed (corresponding to the molten pool). The amount of mole of gas was taken equal to 5.10^{-4} mol of gas, corresponding to an intermediate value between the amount of gas in the boundary layer and in the whole chamber. The two atmospheres ($P = 0.3 \text{ MPa}$) used experimentally were considered: argon and air. As expected, the liquidus temperature calculated under argon (3077 K) is

higher than the one calculated under air (2898 K), in agreement with previous literature works [5,9,43].

The influence of the number of moles of gas on the liquidus temperature and associated O/M ratio of $\text{U}_{0.75}\text{Pu}_{0.25}\text{O}_2$ are illustrated in Fig. 16, by taking values between the boundary layer and the whole chamber.

Under air (in red on Fig. 16), a decrease of the liquidus temperature was noticed when increasing the number of moles of gas. For high amount of gas (10^{-2} and 10^{-1} mol), no liquidus temperature was observed on the solidification paths. For 10^{-3} mol of gas, a liquidus temperature of 2914 K was determined, enhancing the oxidation of the sample and leading thus to an increase of the O/M ratio. These results are in agreement with the measurements of Strach et al., where the melting temperature was found to decrease with the number of successive shots under air [9].

Under argon (in green on Fig. 16), a liquid temperature was observed also for the highest amount of gas studied here. In addition, an increase of the temperature associated with a decrease of the O/M ratio was observed when increasing the number of moles of gas. Indeed, the liquidus temperature is determined at $T = 3050 \text{ K}$ in the case of an equilibrium with the boundary layer, and at $T = 3130 \text{ K}$ for 10^{-2} mol of gas.

Moreover, the liquidus temperature (3050–3060 K) and the O/M ratio (1.95–1.96) remain stable in the range $5.9 \times 10^{-6}\text{--}10^{-4}$ mol of gas. This is in agreement with the reproducibility of the melting temperatures observed by Böhler et al. [5].

As it is not possible to determine experimentally the amount of gas reacting with the samples, the only approach available to determine this quantity is the use of calculations, as performed here. Thus, the range $5.9 \cdot 10^{-6}\text{--}10^{-4}$ mol of gas can be considered as realistic and illustrating accurately the experimental conditions.

5.2.3. Solidification paths

To get further insight into what is happening during cooling, solidification paths for $y = 0.14, 0.46, 0.55$ and 0.62 were calculated with $n = 5 \cdot 10^{-4}$ mol of air (red) and Ar (green) (Fig. 17). The results obtained were compared to the O/M ratio determined by XANES (dashed lines) in section 4.2 after melting under air and Ar (Strach et al. [9]). It is important to note that in this case, the solidus temperatures and O/M ratios determined experimentally are only given as comparison with the modelling predictions and were not used in the re-assessment. The O/M

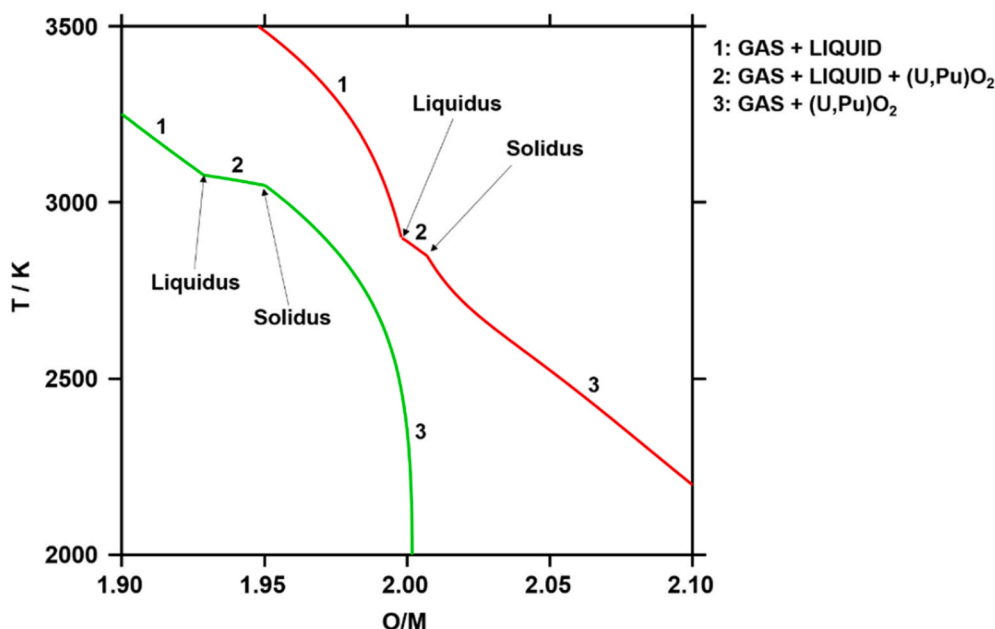


Fig. 15. Solidification paths for $\text{U}_{0.75}\text{Pu}_{0.25}\text{O}_2$ under 10^{-4} mol of gas (red: air – green: argon).

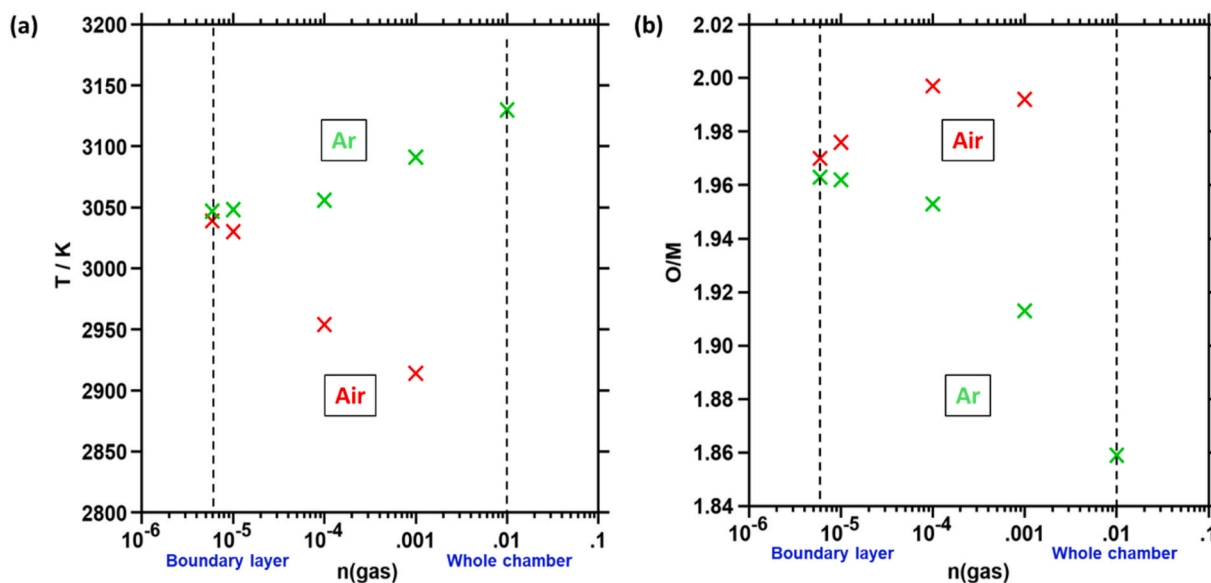


Fig. 16. Variation of the calculated (a) liquidus temperature and (b) O/M ratio for $U_{0.75}Pu_{0.25}O_{2\pm x}$ as a function of the number of moles of gas reacting with the sample (red: air and argon: green).

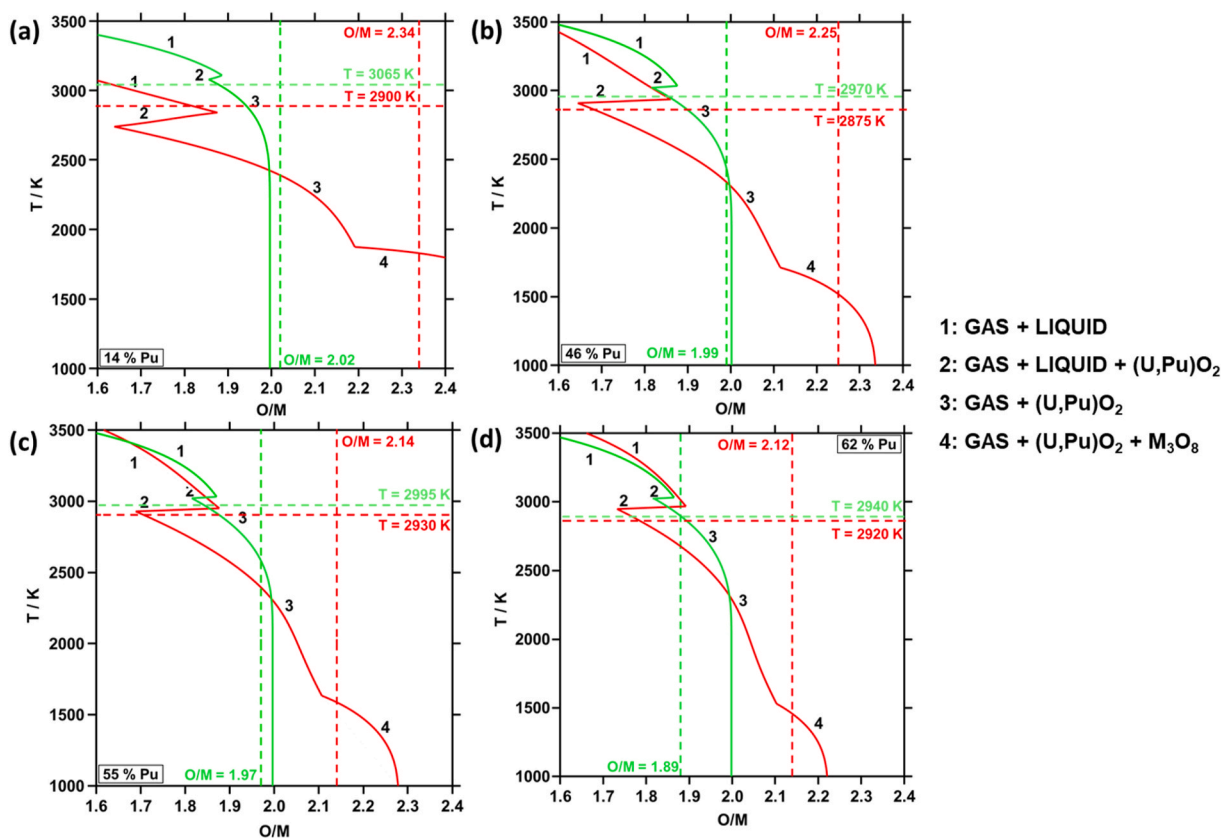


Fig. 17. Calculated solidification paths in air (in red) and argon (in green) for (a) $y = 0.14$, (b) $y = 0.46$, (c) $y = 0.55$ and (d) $y = 0.62$, for 5×10^{-4} mol of gas. The calculations are compared to the experimental results in dashed lines (O/M ratios determined at room temperature by XANES (section 4.2) and the solidus temperatures obtained by Strach et al. [9]).

ratio calculated in the solidification paths corresponds to the global O/M ratio of the sample ($U_{1-y}Pu_yO_{2\pm x}$ and possible other phases).

The calculations indicate that the samples are hypostoichiometric at the solidus and liquidus temperatures regardless of the atmosphere or Pu content, and thus tend to reoxidise during cooling.

In the case of a melting under argon, the samples of $y = 0.14, 0.46$

and 0.55 show a measured O/M ratio close to 2.00 at room temperature. The calculations are in good agreement with these experimental data ($1.97-2.02$), when considering that the samples were reoxidised whilst cooling. According to the calculations, the O/M ratio determined experimentally should be reached at approximately 2500 K. For the highest plutonium content studied here ($y = 0.62$), the O/M ratio

determined at 1.89 could correspond to the composition at the solidus/liquidus temperature, indicating that no reoxidation occurred during the cooling.

As expected, under air, the calculations indicate the important oxidation of the samples during cooling, in agreement with the O/M ratios determined experimentally. According to the calculations, the oxide U_3O_8 could form below 1700 K. This is consistent with the high O/M ratios (2.12–2.34) measured in the present work and the formation of M_3O_8 was already assumed by Strach et al. [9]. The proportion of the M_3O_8 phase increases when increasing the U content. Indeed, Strach et al. measured a quantity bigger for $y = 0.14$ (100 wt %) than for $y = 0.62$ (20 wt %) [44].

According to the calculations, the O/M ratios determined by XANES after the laser heating tests under air are not representative of the O/M ratio at the solidus temperature. Indeed, as already discussed by Epifano et al. [27], uncertainties remain on the oxygen stoichiometry at the solidus/liquidus temperature. In fact, the O/M ratio determined at room temperature corresponds to the one of the entire heat treatment (heating + cooling) and reflect the re-oxidation of the samples occurring during cooling. Nevertheless, these calculations indicate that the O/M ratios observed at room temperature correspond to the one at approximately 1500 K under air and at approximately 2500 K under Ar.

6. Conclusion

As the margin to fuel melting is crucial for the fast reactor design, the prediction of the solid to liquid transitions temperatures of the U–Pu–O system as a function of plutonium and oxygen compositions is mandatory. To this aim, the thermodynamic model of the Pu–O and U–Pu–O systems of Guéneau et al. [7] was improved to take into account the recent sets of experimental data.

First, a critical review of the available experimental data was performed, highlighting important discrepancies between the various techniques used for the determination of the melting points. Based on this review, experimental data were chosen for the re-assessment of the models of the Pu–O and U–Pu–O systems. The parameters of the liquid phase for the two systems were re-evaluated using the CALPHAD method. Overall, a good agreement between the selected experimental data and the calculated data was obtained. The complex melting behaviour of $U_{1-y}Pu_yO_{2\pm x}$ mixed oxides was highlighted, confirming that UO_2 – PuO_2 is not a pseudo-binary system. The congruent melting was found to be shifted towards lower O/M ratio for $U_{1-y}Pu_yO_{2-x}$ (1.90) compared to the end-members ($UO_{1.97}$ and $PuO_{1.95}$). This was explained by the stabilisation of the mixed oxide in the hypo-stoichiometric region ($O/M < 2$), due to the increase of the configurational entropy by the formation of oxygen vacancies and increasing Pu^{3+}/Pu^{4+} disorder occurring at high temperature.

This reassessed model was then used to calculate solidification paths for samples molten by laser heating under both argon and air. The influence of the amount of gas reacting with the sample was discussed and it was evidenced that a limited amount of gas was reacting with the sample.

In the present work, O/M ratios of post-melted samples were also

determined by X-Ray Absorption Spectroscopy (XANES). An oxidation of the samples was noticed for the samples molten under air, whereas a reduction was observed under argon. The simultaneous presence of U^{4+} , U^{5+} , U^{6+} , Pu^{3+} and Pu^{4+} was also evidenced, highlighting partial charge compensation mechanisms. These O/M ratios determined experimentally were compared to calculated solidification paths. In the case of air, the samples were highly oxidised with $O/M > 2$ with the formation of U_3O_8 , while the O/M ratios of the samples molten under argon were slightly hypo-stoichiometric or close to 2. The calculations suggested that a reoxidation of the samples occurred during cooling. Thus, the exact O/M ratio at which the solidus and liquidus temperatures are measured remain unknown. Further experimental work with in-situ measurement of the oxygen release and absorption of the samples would be helpful to conclude on this point.

This updated model of the U–Pu–O system will allow a better description of higher order systems such as U–Pu–MA–FP–O systems (MA = minor actinides, FP = fission products), to predict the high temperature behaviour of the fuel materials in Sodium-cooled Fast Reactors. The current results will be further taken into account in the Fuel Performance Codes in order to improve the models for the margin to fuel melting as well as the thermal conductivity.

Although experimental data are available on the high-plutonium range of the U–Pu–O system, this work highlights the need to perform new experimental campaigns. Moreover, the determination of the O/M ratio during the melting represents a real challenge and dedicated experimental studies are needed. These new data would help validating the current models and thus reducing the uncertainties on the margin to fuel melting.

Declaration of competing interest

The authors declare that they have no known competing financial interests or personal relationships that could have appeared to influence the work reported in this paper.

Data availability

Data will be made available on request.

Acknowledgments

This work was supported by the Cross-cutting basic research Program (RTA Program) of the CEA Energy Division. This work has received funding from the Euratom research and training programme 2014–2018 through the INSPYRE project under grant agreement No 754329. The KIT synchrotron light source is also acknowledged for the use of the INE-Beamline at the Karlsruhe Research Accelerator (KARA). M. Sierig, D. Prieur and the JRC-Karlsruhe technical staff are acknowledged for their help in the sample preparation for the XANES measurements. The authors also acknowledged R. Belin for his contribution. P. Fouquet-Métivier thanks the ENEN+European H2020 project (grant agreement No 755576) for funding a mobility at the JRC Karlsruhe.

Appendix A. Supplementary data

Supplementary data to this article can be found online at <https://doi.org/10.1016/j.calphad.2022.102523>.

Appendix

Table 3

Pu content, solidus and liquidus temperatures, O/M before and after the melting of the samples used for the re-assessment of the model of the U-Pu-O system.

Reference	y (Pu content in $U_{1-y}Pu_yO_{2\pm x}$)	O/M ratio before melting	Solidus temperature (K)	Liquidus temperature	O/M ratio after melting	
Böhler et al. [5]	0	2.00	3126 ± 55		2.00	
	0.037	2.00	3107 ± 55	3129 ± 55	2.00	
	0.09	2.00	3097 ± 55	3116 ± 55	2.00	
	0.25	2.00	3015 ± 55	3052 ± 55	2.00	
	0.40	2.00	2993 ± 55	3015 ± 55	2.00	
	0.50	2.00	2985 ± 55	3007 ± 55	2.00	
	0.80	2.00	3023 ± 55	3023 ± 55	2.00	
	0.90	2.00	3012 ± 55	3037 ± 55	2.00	
	1	2.00	3050 ± 55		2.00	
	Kato et al. [23]	0	2.00	3140 ± 9	3145 ± 16	2.00
2.00			3111 ± 9	3130 ± 16	2.00	
0.118		2.00	3134 ± 9	3173 ± 16	2.00	
		2.00	3077 ± 9	3117 ± 16	2.00	
			3093 ± 9	3135 ± 16	2.00	
			3084 ± 9	3105 ± 16	2.00	
		1.989	3093 ± 20	3135 ± 55	1.989	
		1.983	3084 ± 20	3105 ± 55	1.983	
		1.975	3085 ± 20	3107 ± 55	1.975	
		1.971	3100 ± 20	3124 ± 55	1.971	
		0.199	2.00	3052 ± 9	3090 ± 16	2.00
				3059 ± 9	3089 ± 16	2.00
		1.982	3059 ± 20	3089 ± 55	1.982	
		1.967	3066 ± 20	3079 ± 55	1.967	
		1.954	3074 ± 20	3109 ± 55	1.954	
		1.954	3079 ± 20	3097 ± 55	1.954	
		1.942	3092 ± 20	3118 ± 55	1.942	
0.298		2.00	3030 ± 9	3074 ± 16	2.00	
0.397		2.00	2997 ± 9	3117 ± 16	2.00	
			3009 ± 9	3020 ± 16	2.00	
		1.972	3035 ± 20	3071 ± 55	1.972	
		1.959	3025 ± 20	3037 ± 55	1.959	
	1.925	3073 ± 20	3102 ± 55	1.925		

Table 4

Interaction parameters of the liquid phase of the Pu-O system.

Parameters	Previous version (2011)	New version (2021)
G(Liq,Pu ³⁺ :O ²⁻ ;0) -3.H ²⁹⁸ (O)-2.H ²⁹⁸ (Pu)	+GPU2O3 + 113 000-47.9219678*T	+GPU2O3 +72 000-30.187*T
G(Liq,PuO ₂ ;0) -2.H ²⁹⁸ (O)-H ²⁹⁸ (Pu)	+GPUO2 + 67 000-22.2*T	+GPUO2 + 68 320-22.3*T
L(Liq,Pu ³⁺ :O ²⁻ ,Va;0)	77 451.8 + 23.4798*T - 20 231.6*(yO ₂ - yVa)	77451.8 + 23.4798*T
L(Liq,Pu ³⁺ :O ²⁻ ,Va;1)	-	-20231.6
L(Liq,Pu ³⁺ :O ²⁻ ,PuO ₂ ;0)	+60 000-20 000 (yO ₂ - yPuO ₂)	+60 000

Table 5

Interaction parameters of the liquid phase of the U-Pu-O system.

Parameters	Previous version (2011)	New version (2021)
L(Liq,Pu ³⁺ ,U ⁴⁺ :O ²⁻ ;0)	-20 000	-
L(Liq,Pu ³⁺ ,U ⁴⁺ :O ²⁻ ,Va;0)	-	480 000-670*T
L(Liq,U ⁴⁺ :O ²⁻ ,PuO ₂ ;0)	-10 000	1 075 600-360*T
L(Liq,U ⁴⁺ :O ²⁻ ,PuO ₂ ;1)	-	-55 000
L(Liq,Pu ³⁺ ,U ⁴⁺ :O ²⁻ ,PuO ₂ ;0)	+80 000	-

References

- [1] GIF portal - sodium-cooled fast reactor (SFR). https://www.gen-4.org/gif/jcms/c_42152/sodium-cooled-fast-reactor-sfr.
- [2] R.J.M. Konings, D. Haas, Fuels and targets for transmutation, *Compt. Rendus Phys.* 3 (7) (Sep. 2002) 1013-1022, [https://doi.org/10.1016/S1631-0705\(02\)01382-8](https://doi.org/10.1016/S1631-0705(02)01382-8).
- [3] E.A. Aitken, S.K. Evans, A Thermodynamic Data Program Involving Plutonia and Urania at High Temperatures, *Quarterly Rep.* 4 (1968).
- [4] M. Kato, K. Morimoto, H. Sugata, K. Konashi, M. Kashimura, T. Abe, Solidus and liquidus of plutonium and uranium mixed oxide, *J. Alloys Compd.* 452 (1) (Mar. 2008) 48-53, <https://doi.org/10.1016/j.jallcom.2007.01.183>.
- [5] R. Böhler, et al., Recent advances in the study of the UO₂-PuO₂ phase diagram at high temperatures, *J. Nucl. Mater.* 448 (1-3) (May 2014) 330-339, <https://doi.org/10.1016/j.jnucmat.2014.02.029>.
- [6] C. Guéneau, et al., TAF-ID: an international thermodynamic database for nuclear fuels applications, *Calphad* 72 (Mar. 2021), 102212, <https://doi.org/10.1016/j.calphad.2020.102212>.
- [7] C. Guéneau, et al., Thermodynamic modelling of advanced oxide and carbide nuclear fuels: description of the U-Pu-O-C systems, *J. Nucl. Mater.* 419 (1-3) (Dec. 2011) 145-167, <https://doi.org/10.1016/j.jnucmat.2011.07.033>.

- [8] F. De Bruycker, et al., On the melting behaviour of uranium/plutonium mixed dioxides with high-Pu content: a laser heating study, *J. Nucl. Mater.* 419 (1) (Dec. 2011) 186–193, <https://doi.org/10.1016/j.jnucmat.2011.08.028>.
- [9] M. Strach, D. Manara, R.C. Belin, J. Rogez, Melting behavior of mixed U–Pu oxides under oxidizing conditions, *Nucl. Instrum. Methods Phys. Res. Sect. B Beam Interact. Mater. Atoms* 374 (May 2016) 125–128, <https://doi.org/10.1016/j.nimb.2016.01.032>.
- [10] Inspyre - investigations supporting MOX fuel licensing in ESNII prototype reactors. <http://www.eera-jpnm.eu/inspyre/index.php>.
- [11] J.J. Carbajo, G.L. Yoder, S.G. Popov, V.K. Ivanov, A review of the thermophysical properties of MOX and UO₂ fuels, *J. Nucl. Mater.* 299 (3) (Dec. 2001) 181–198, [https://doi.org/10.1016/S0022-3115\(01\)00692-4](https://doi.org/10.1016/S0022-3115(01)00692-4).
- [12] F. De Bruycker, K. Boboridis, P. Pöml, R. Eloirdi, R.J.M. Konings, D. Manara, The melting behaviour of plutonium dioxide: a laser-heating study, *J. Nucl. Mater.* 416 (1) (Sep. 2011) 166–172, <https://doi.org/10.1016/j.jnucmat.2010.11.030>.
- [13] D. Manara, M. Sheindlin, W. Heinz, C. Ronchi, New techniques for high-temperature melting measurements in volatile refractory materials via laser surface heating, *Rev. Sci. Instrum.* 79 (11) (Nov. 2008), 113901, <https://doi.org/10.1063/1.3005994>.
- [14] R.J.M. Konings, et al., The thermodynamic properties of the *f*-elements and their compounds. Part 2. The lanthanide and actinide oxides, *J. Phys. Chem. Ref. Data* 43 (1) (Mar. 2014), 013101, <https://doi.org/10.1063/1.4825256>.
- [15] M. Kato, et al., Effect of oxygen-to-metal ratio on melting temperature of uranium and plutonium mixed oxide fuel for fast reactor, *Trans. Atom. Energy Soc. Jpn.* 7 (Dec. 2008) 420–428, <https://doi.org/10.3327/taesj.J08.001>.
- [16] F. De Bruycker, K. Boboridis, D. Manara, P. Pöml, M. Rini, R.J.M. Konings, Reassessing the melting temperature of PuO₂, *Mater. Today* 13 (11) (Nov. 2010) 52–55, [https://doi.org/10.1016/S1369-7021\(10\)70204-2](https://doi.org/10.1016/S1369-7021(10)70204-2).
- [17] T.D. Chikalla, C.E. McNeilly, R.E. Skavdahl, The plutonium-oxygen system, *J. Nucl. Mater.* 12 (2) (Jul. 1964) 131–141, [https://doi.org/10.1016/0022-3115\(64\)90132-1](https://doi.org/10.1016/0022-3115(64)90132-1).
- [18] B. Riley, High temperature oxygen equilibrium in the PLUTONIUM–OXYGEN system, *Jan. 1970, Sci. Ceram.* 5 (1970) 83–109. Available: <https://www.osti.gov/biblio/4085857>.
- [19] M. Kato, K. Morimoto, H. Sugata, K. Konashi, M. Kashimura, T. Abe, Solidus and liquidus temperatures in the UO₂–PuO₂ system, *J. Nucl. Mater.* 373 (1) (Feb. 2008) 237–245, <https://doi.org/10.1016/j.jnucmat.2007.06.002>.
- [20] W.L. Lyon, W.E. Baily, The solid-liquid phase diagram for the UO₂–PuO₂ system, *J. Nucl. Mater.* 22 (3) (Jun. 1967) 332–339, [https://doi.org/10.1016/0022-3115\(67\)90051-7](https://doi.org/10.1016/0022-3115(67)90051-7).
- [21] J.G. Reavis, Los Alamos Scientific Lab, LA-5193-PR, 1972.
- [22] K. Konno, T. Hirotsawa, Melting temperature of irradiated fast reactor mixed oxide fuels, *J. Nucl. Sci. Technol.* 35 (7) (Jul. 1998) 494–501, <https://doi.org/10.1080/18811248.1998.9733897>.
- [23] M. Kato, Melting temperatures of oxide fuel for fast reactors, in: *International Congress on Advances in Nuclear Power Plants 2009*, vol. 3, Jan. 2009, pp. 1940–1947. ICAPP 2009.
- [24] K. Konno, T. Hirotsawa, Melting temperature of irradiated fast reactor mixed oxide fuels, *J. Nucl. Sci. Technol.* 35 (7) (Jul. 1998) 494–501, <https://doi.org/10.1080/18811248.1998.9733897>.
- [25] M.G. Adamson, E.A. Aitken, R.W. Caputi, Experimental and thermodynamic evaluation of the melting behavior of irradiated oxide fuels, *J. Nucl. Mater.* 130 (Feb. 1985) 349–365, [https://doi.org/10.1016/0022-3115\(85\)90323-X](https://doi.org/10.1016/0022-3115(85)90323-X).
- [26] D. Manara, C. Ronchi, M. Sheindlin, M. Lewis, M. Brykin, Melting of stoichiometric and hyperstoichiometric uranium dioxide, *J. Nucl. Mater.* 342 (1) (Jun. 2005) 148–163, <https://doi.org/10.1016/j.jnucmat.2005.04.002>.
- [27] E. Epifano, et al., Melting behaviour of uranium-americiem mixed oxides under different atmospheres, *J. Chem. Therm.* 140 (Jan. 2020), 105896, <https://doi.org/10.1016/j.jct.2019.105896>.
- [28] H.L. Lukas, S.G. Fries, B. Sundman, Computational Thermodynamics, The Calphad Method, 2007, <https://doi.org/10.1017/CBO9780511804137>.
- [29] Thermo-calc software - computational materials engineering. <https://www.thermo-calc.com/>.
- [30] M. Kurata, Thermodynamic assessment of the Pu-U, Pu-Zr, and Pu-U-Zr systems, *Calphad* 23 (3) (Sep. 1999) 305–337, [https://doi.org/10.1016/S0364-5916\(00\)00004-3](https://doi.org/10.1016/S0364-5916(00)00004-3).
- [31] M. Hillert, B. Jansson, B. Sundman, J. Ågren, A two-sublattice model for molten solutions with different tendency for ionization, *MTA* 16 (1) (Jan. 1985) 261–266, <https://doi.org/10.1007/BF02815307>.
- [32] C. Guéneau, C. Chatillon, B. Sundman, Thermodynamic modelling of the plutonium–oxygen system, *J. Nucl. Mater.* 378 (3) (Sep. 2008) 257–272, <https://doi.org/10.1016/j.jnucmat.2008.06.013>.
- [33] H.A. Wriedt, The O-Pu (Oxygen-Plutonium) system, *Bull. Alloy Phase Diagr.* 11 (Apr. 1990) 184–202, <https://doi.org/10.1007/BF02841705>.
- [34] P. Gotcu-Freis, J.-Y. Colle, J.-P. Hiernaut, O. Beneš, C. Guéneau, R.J.M. Konings, A mass spectrometric investigation of the vaporisation behaviour in the (U+Pu+O) system, *J. Chem. Therm.* 71 (Apr. 2014) 212–220, <https://doi.org/10.1016/j.jct.2013.12.004>.
- [35] T. Truphémus, et al., Structural studies of the phase separation in the UO₂–PuO₂–Pu₂O₃ ternary system, *J. Nucl. Mater.* 432 (1–3) (2013), <https://doi.org/10.1016/j.jnucmat.2012.07.034>. Art. no. 1–3, Jan.
- [36] J. Rothe, et al., The INE-Beamline for actinide science at ANKA, *Rev. Sci. Instrum.* 83 (4) (Apr. 2012), 043105, <https://doi.org/10.1063/1.3700813>.
- [37] B. Ravel, M. Newville, ATHENA, artemis, hephaestus: data analysis for X-ray absorption spectroscopy using IFEFFIT, *J. Synchrotron Radiat.* 12 (4) (2005), <https://doi.org/10.1107/S0909049505012719>. Art. no. 4, Jul.
- [38] K.O. Kvashnina, S.M. Butorin, P. Martin, P. Glatzel, Chemical state of complex uranium oxides, *Phys. Rev. Lett.* 111 (25) (Dec. 2013), 253002, <https://doi.org/10.1103/PhysRevLett.111.253002>.
- [39] K. Popa, et al., Structural investigations of PuIII phosphate by X-ray diffraction, MAS-NMR and XANES spectroscopy, *J. Solid State Chem.* 230 (Oct. 2015) 169–174, <https://doi.org/10.1016/j.jssc.2015.07.002>.
- [40] D. Prieur, et al., Accommodation of multivalent cations in fluorite-type solid solutions: case of Am-bearing UO₂, *J. Nucl. Mater.* 434 (1–3) (Mar. 2013) 7–16, <https://doi.org/10.1016/j.jnucmat.2012.11.037>.
- [41] D. Prieur, et al., Local structure and charge distribution in mixed uranium–americium oxides: effects of oxygen potential and Am content, *Inorg. Chem.* 50 (24) (Dec. 2011) 12437–12445, <https://doi.org/10.1021/ic200910f>.
- [42] A. Quaini, et al., High temperature investigation of the solid/liquid transition in the PuO₂–UO₂–ZrO₂ system, *J. Nucl. Mater.* 467 (Dec. 2015) 660–676, <https://doi.org/10.1016/j.jnucmat.2015.10.007>.
- [43] F. De Bruycker, High Temperature Phase Transitions in Nuclear Fuels for the Fourth Generation, Université d’Orléans, 2010.
- [44] M. Strach, R.C. Belin, J.-C. Richaud, J. Rogez, High temperature X-ray diffraction study of the oxidation products and kinetics of uranium–plutonium mixed oxides, *Inorg. Chem.* 53 (24) (Dec. 2014) 12757–12766, <https://doi.org/10.1021/ic501580x>.